



UNIVERSIDAD
DE CANTABRIA

FACULTAD DE CIENCIAS

**OPTIMIZATION OF THE GEOMETRY OF
DOMESTIC GAS BURNER INJECTORS BY
USING THE DESIGN EXPLORATION PROCESS**

(Optimización de la geometría de los inyectores de los quemadores de gas domésticos utilizando el proceso de Exploración de Diseño)

TRABAJO DE FIN MÁSTER PARA ACCEDER AL
MÁSTER EN MATEMÁTICAS Y COMPUTACIÓN

AUTORA: ADRIANA CAVADA LÓPEZ-TAPIA

DIRECTOR: LUIS ALBERTO FERNÁNDEZ FERNÁNDEZ

CO-DIRECTOR: JOSÉ SALVADOR OCHOA TORRES

SANTANDER, FEBRERO DE 2019

Resumen

En un quemador de gas doméstico, el injector es el elemento que controla la entrada de flujo másico. Dentro de este dispositivo, el gas sufre una caída de presión debido a la descarga de un caudal a través de un orificio calibrado. A la salida, el chorro resultante sale a alta velocidad y arrastra el aire de su alrededor mezclándolo con el gas. El objetivo fundamental de este proyecto es analizar la influencia que tiene la geometría interna de los inyectores en el comportamiento del chorro de combustible y su capacidad de arrastre. El diámetro interno de un inyector controla la mayoría de la caída de presión y, por lo tanto, es el parámetro más relevante para definir el caudal. Este estudio se centrará en los otros dos parámetros principales de los inyectores, a saber, la altura de la garganta del inyector, h , y el ángulo que forma con la zona de convergencia, α . Para llevar a cabo de manera eficiente el estudio se ha seguido el proceso de Exploración del Diseño, utilizando un módulo llamado DesignXplorer que es parte del software comercial ANSYS. Como parte del proceso también se han analizado las diferentes herramientas matemáticas involucradas en el mismo, como son, los Diseños de Experimentos (DOEs), los algoritmos de generación de Superficies de Respuesta o los diferentes métodos para el proceso de optimización.

Se han simulado un total de 149 geometrías de inyector que forman parte de tres tipos diferentes de DOEs. El algoritmo elegido para la generación de las Superficies de Respuesta ha sido el de Agregación Genética. Para la optimización multi-objetivo se ha utilizado un método genético llamado MOGA (Multi-Objective Genetic Algorithm), con el objetivo de maximizar al mismo tiempo el arraste de aire y el coeficiente de descarga del inyector. Como veremos, este proceso muestra que los mejores resultados los proporcionan alturas pequeñas ($h \in [0.25, 1.75]$ veces el diámetro) y ángulos grandes ($\alpha \in [155, 160]^\circ$).

Por último, entre los DOEs que hemos probado, se ha visto que lo más eficiente es dividir de forma uniforme el espacio de muestreo y, como cabía esperar, el número de puntos de diseño es el factor que más afecta a la calidad de los resultados.

Palabras clave: proceso de exploración del diseño, diseño de experimentos, superficie de respuesta, optimización multi-objetivo, inyector de gas, quemador doméstico.

Abstract

In domestic gas burners, the injector is the element that controls the fuel mass flow rate. Inside this device, an over-pressured gas undergoes a pressure drop due to a flow discharge through a calibrated orifice. At the exit, the resulting high-speed jet is responsible for entraining the surrounding air for premixing purposes. The fundamental aim of this project is to analyze the influence of the internal geometry of gas burner injectors on the performance of the fuel jet and its capacity to entrain air. The internal orifice diameter of an injector manages most of the pressure drop and therefore it is also usually the most relevant parameter to define a targeted mass flow rate. This study will focus on the other two main parameters of injectors, namely, the height of the nozzle throat, h , and the angle of the convergent zone, α . The Design Exploration process has been followed to efficiently carry out this study, using a module called DesignXplorer, part of the commercial software ANSYS. As a part of the process, we also have analyzed the mathematical tools involved, *i.e.* the Design of Experiments (DOEs), the Response Surface algorithms or the different optimization methods.

We have simulated a total of 149 injector geometries, forming part of three different types of DOEs. The Genetic Aggregation algorithm has been chosen for Response Surfaces generation. For the multi-objective optimization, we have used the MOGA (Multi-Objective Genetic Algorithm) method, with the target of maximizing the air entrainment and, at the same time, the discharge coefficient. This approach has shown that small heights ($h \in [0.25, 1.75]$ times the diameter) with larger angles ($\alpha \in [155, 160]^\circ$) give better results.

Finally, among the tested DOEs, we have seen that the uniform distribution of design points is the best option considering the quality metrics, although the number of them is the most affecting variable.

Key words: *design exploration process, design of experiments, reponse surface, multi-objective optimization, gas injector, domestic gas burner.*

Contents

Resumen	ii
Abstract	iii
Contents	iv
1 Introduction	1
1.1 Purpose	1
1.2 Motivation	2
1.3 Software	3
1.4 Framework	5
2 Background Theory	6
2.1 Governing PDE's	6
2.1.1 Navier-Stokes equations	6
2.1.2 Chemical species conservation	7
2.1.3 Energy conservation	8
2.2 Turbulence modeling	9
2.3 $k - \varepsilon$ model	9
2.4 Aerated gas burners	10
2.4.1 Structure and performance of domestic burners	11
2.5 Flow passing an injector	12
2.5.1 Coefficient of discharge	13
2.6 Air entrainment	14
2.6.1 Aeration	14
3 Optimization Theory	16
3.1 Introduction to Design Exploration	16

3.2	Design Of Experiments (DOE)	17
3.2.1	Terminology	17
3.2.2	DOE Types	18
3.3	Response Surface	20
3.3.1	Response Surface Techniques	20
3.3.2	Refinement Points	23
3.4	Quality Metrics	23
3.4.1	Goodness of Fit (GOF)	23
3.4.2	Verification Points (VP)	25
3.5	Optimization	26
4	Case configuration	28
4.1	Description of the case	28
4.1.1	Geometry	28
4.1.2	Boundary conditions	30
4.1.3	Mesh	30
4.2	DOE configurations	32
5	Results	34
5.1	DOE quality metrics	34
5.2	Custom DOE - 36 runs	37
5.2.1	Local Sensitivities	38
5.2.2	Response Surfaces	39
5.2.3	Optimization	46
6	Concluding remarks	50
6.1	Conclusions	50
6.2	Future work	52
Appendices		vi
A	Fluid concepts	vi
A.1	Fluid numbers	vi
A.2	Diffusive fluxes	viii
Nomenclature		ix
Bibliography		xiv

Chapter 1

Introduction

The beginning is half of everything.

Pythagoras of Samos

1.1 Purpose

In domestic gas burners, the injector is the element that controls the fuel mass flow rate. Inside this device, an over-pressured gas undergoes a pressure drop due to a flow discharge through a calibrated orifice. At the exit, the resulting high-speed jet is responsible for entraining the surrounding air for premixing purposes.

The fundamental objective of this project is to analyze the influence of the internal geometry of gas burner injectors on the performance of the fuel jet and its capacity to entrain air. The internal orifice diameter of an injector handles most of the pressure drop and therefore it is also usually the most relevant parameter to define a targeted mass flow rate. This study will focus on the other two parameters of injectors, namely the height of the nozzle and the angle of the convergent zone (see Figure 1.1). After studying a reference-base case, the process uses an optimization method to find injector configurations that meet some physical constraints sought in the gas burner design (such as maximizing air entrainment, for example).

In order to efficiently carry out the parametric analysis, the so-called *Design Exploration process* is followed. The first step in the process is to determine ranges within the dimensions will vary, forming our sampling space. The next step is to solve each different configuration and recollect a battery of data from which getting the response surfaces that relate the input parameters

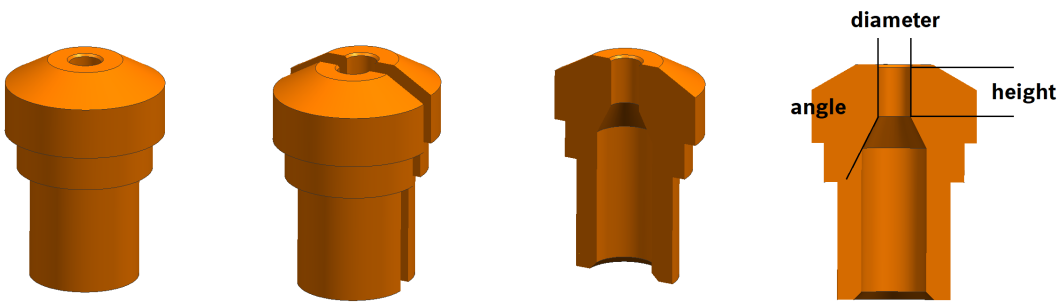


Figure 1.1 – Geometry of a domestic gas burner injector. It shows the three main geometric variables: the diameter, the height of the throat and the angle it forms with the entry of gas.

with the output physical variables. Once this is done, the last step is to use an optimization method that looks for the optimal points that meet the required restrictions.

As part of this study, we also analyze the mathematical tools involved in the Design Exploration (DE) process to integrate it in the future development procedure of new burners. The different Design of Experiments (DOE) are analyzed to determine the efficiency of each one; also the existing algorithms to generate the Response Surfaces (RS) will be studied, and finally, the available optimization methods will be investigated. A commercial software called ANSYS [2] is used for this project.

1.2 Motivation

With sufficient time and resources, it would not be probably necessary to devote efforts to studying the design of experiments. However, this is not the case either in real life or in the manufacturing sector, where we have to anticipate errors in the production process relying on the underlying theory to finally reduce costs and improve efficiency. From an engineering point of view, there is always a requirement to improve any process. To do so, optimal and well-designed experiments considering as much as possible modifications are essential. This process needs to be robust and focus on conclusions rather than possible experimental errors.

DE is a particular way of arriving at an optimal design solution (Figure 1.2). It is a powerful approach to exploring, understanding and optimizing engineering challenges. Enough information is gathered about the current design to answer what-if questions that quantify the influence of design variables on product performance. By doing so, decisions are based on accurate information, even with an unexpected change in the design constraints. We could see DE as an evolution beyond the traditional process of design optimization.

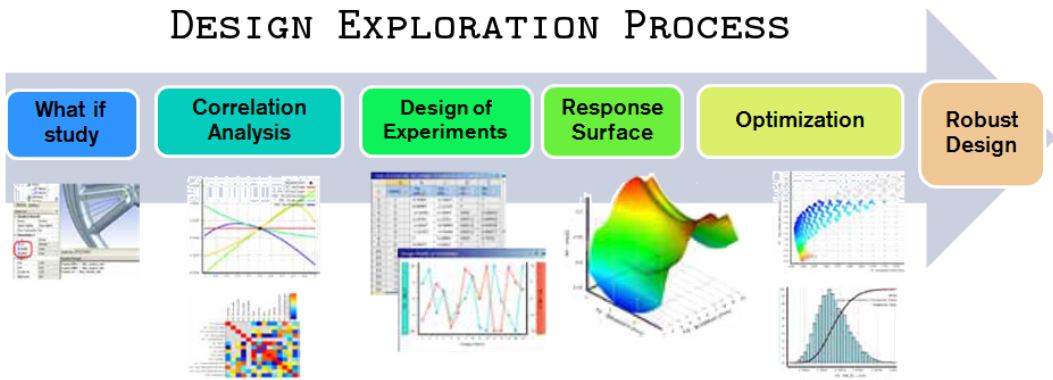


Figure 1.2 – Design Exploration process.

One of the main advantages of applying a DE technique is that it is cheaper than any optimization algorithm as it requires fewer samples. However, one drawback of the process is that the result is a response surface that can be an approximation or an interpolation, and knowing the quality of the adjustment and future extrapolation is not an easy task.

Possibly the greatest limitation to the late development of the DE technique has been the accessibility of the software as learning about design exploration can be a rather difficult task because of the multi-disciplinarity of the process. Topics, as varied as CAD, probability or optimization techniques, are needed and are not usually part of the common engineering curriculum. However, DE is increasingly used in many industries to speed up and improve the development of new products and processes. When applied correctly, it can reduce time to market, development and production costs, and improve quality and reliability.

Besides the DE, it is a necessity to use the computational simulation (Figure 1.3). It is totally unrealistic to handle a hundred or more experiments, each of them with a different geometry, in order to study their different behaviors. Such a procedure would be really hard and costly if made by prototyping, so the use of numerical simulation appears to be the best solution.

Summing up, numerical simulation along with the DE allow us to perform the best possible study of the case proposed in this document. Simulation is necessary to reproduce the behavior of cases as if we were in a laboratory but in a cheaper way, and the design of experiments is used to explore the sampling space in an efficient and effective mode.

1.3 Software

We will use a commercial simulation software called ANSYS [2]. It offers a comprehensive suite of simulation solvers that spans a range of physics, providing access to virtually any field of

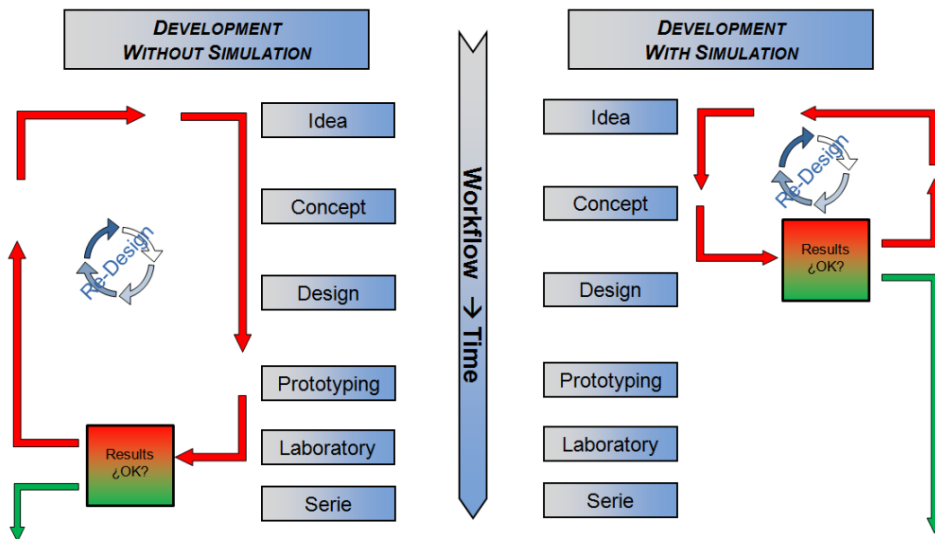


Figure 1.3 – Inclusion of Simulation in the Development Process. Source: [9]

engineering simulation that a design process requires. ANSYS handles geometry, mesh, and DE process (which is called DesignXplorer). The latter is used to solve the different Design of Experiments, create the response surfaces of outputs, and finally find points that optimize the injector geometries. Figure 1.4 shows the project general scheme as it appears in ANSYS.

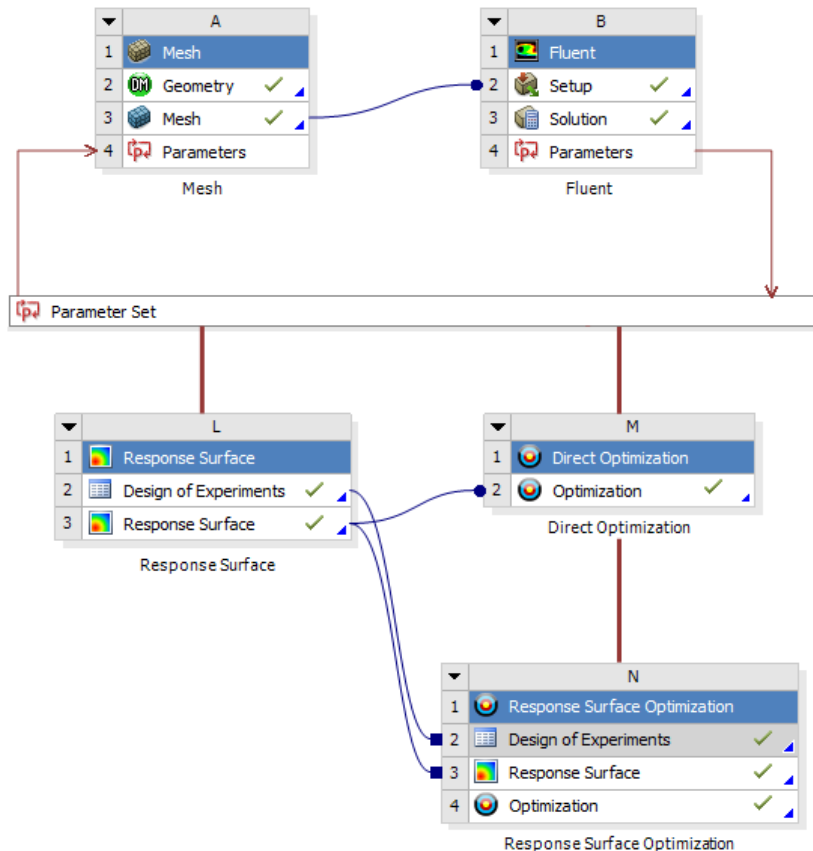


Figure 1.4 – ANSYS project workflow.

1.4 Framework

This final project of the master is a collaboration between the Department of Predevelopment of the company BSH Home Appliances Group and the Department of Mathematics, Statistics and Computing of the University of Cantabria. This project was carried out as part of the simulation team at the BSH Santander plant, which specializes in the development and manufacture of gas cooktops.

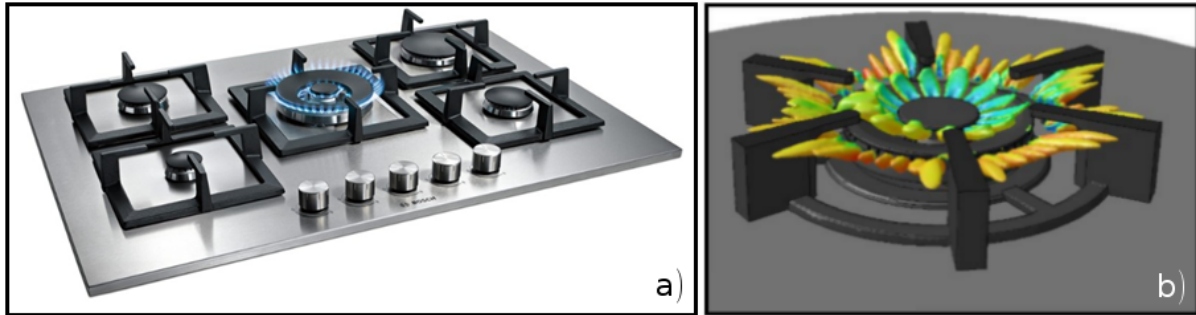


Figure 1.5 – a) Gas hob manufactured in BSH Santander. b) Image from a combustion simulation of the BSH wok. *Source: [9]*

This study is relevant since the influence of the internal shape of an injector on the fuel jet could affect not only the power rate but also the amount of air entrainment and, finally, the burner performance. Although it is well known that the diameter of the injector throat is the most influencing variable, there is also some pressure losses associated with other geometric variables. So far, traditional injector design is based on a trial-and-error sequence. Pressure losses are associated to a so-called discharge coefficient to match theoretical to reference or experimental power rate. This process is made cyclically up to find the right configuration. By simulation, it is possible to test several injector configurations and find the geometrical dependences on the discharge coefficients. Having a better estimation of this coefficient, burner designers might have faster and more right designs of the injector nozzles. On context, with the analysis of the exploration process, in the future, we would have the knowledge to efficiently prepare parametric studies involving other technologies. Analyzing in depth each of the mathematical tools used by the process, we would know how to adapt each of them and how to choose one or the other in new cases as it best suits.

Chapter 2

Background Theory

I would give everything I know for half of what I ignore.

René Descartes

2.1 Governing PDE's

The evolution of a mixed-gas system is governed by the flow dynamics, the chemical reactions and the turbulence modeling. This set of transport equations represent the conservation of mass, momentum, energy and chemical species. These governing equations as well as some important concepts related with the physics of domestic burners are briefly described in this chapter. For more in-depth scientific detail the reader may consult [20] or [29] for example.

2.1.1 Navier-Stokes equations

Mass and momentum conservation are described by the well-known Navier-Stokes equations.

The PDE of the mass conservation is the called *continuity equation*

$$\frac{\partial \rho}{\partial t} + \nabla \cdot (\rho \mathbf{v}) = 0, \quad (2.1)$$

where ρ is the density of the mixture and \mathbf{v} the velocity vector. Usually in most combustion problems the density is calculated using the ideal gas law

$$\rho = \frac{p \overline{M}}{R T}, \quad (2.2)$$

with R being the universal gas constant, p the total pressure, T the temperature and \bar{M} the average molecular weight of the mixture. The latter defined as follows:

$$\bar{M} = \left(\sum_{\alpha=1}^{N_\alpha} \frac{Y_\alpha}{M_\alpha} \right)^{-1}, \quad (2.3)$$

where Y_α and M_α are the mass fraction and the average molecular weight of the α species respectively.

On the other hand, the momentum conservation is derived from the Newton's Second Law and it is described by the following equation:

$$\frac{\partial}{\partial t}(\rho \mathbf{v}) + \nabla \cdot (\rho \mathbf{v} \mathbf{v}) = -\nabla p + \nabla \cdot \boldsymbol{\tau} + \rho \mathbf{f}, \quad (2.4)$$

where \mathbf{f} are the body forces acting on the fluid and $\boldsymbol{\tau}$ is the viscous stress tensor related with the surface forces. Gravitational acceleration, \mathbf{g} , is the only body force to take into account in the case presented in this project.

Since the mixture of gases can be considered as a Newtonian fluid, the stress tensor can be expressed as follows

$$\boldsymbol{\tau} = \mu (\nabla \mathbf{v} + (\nabla \mathbf{v})') - \frac{2}{3} \mu (\nabla \cdot \mathbf{v}) \mathbf{I}, \quad (2.5)$$

with μ being the dynamic viscosity and \mathbf{I} the identity tensor.

2.1.2 Chemical species conservation

The mass fraction of a chemical species, Y_α in a mixture of N_α species is

$$Y_\alpha = \frac{m_\alpha}{m_T}, \quad (2.6)$$

where m_α is the mass of the α species and m_T is the total mass of the mix. In terms of the mass fraction, the species conservation for a single species is as follows:

$$\frac{\partial}{\partial t}(\rho Y_\alpha) + \nabla \cdot (\rho \mathbf{v} Y_\alpha) = -\nabla \cdot \mathbf{J}_\alpha + S_\alpha, \quad \alpha = 1, \dots, N_\alpha; \quad (2.7)$$

where \mathbf{J}_α is the diffusive flux¹ of α species and S_α is the net formation of the α species.

¹See appendix A for more information.

2.1.3 Energy conservation

In the general case, total energy in a fluid volume is the sum of internal energy u , kinetic energy K , and potential energy U ,

$$E = u + K + U. \quad (2.8)$$

By introducing the relation of internal energy and enthalpy H ,

$$u = \frac{H + pV}{m_T}, \quad (2.9)$$

the conservation equation for the energy can be described with the following enthalpy transport equation, with V being the volume of the mixture:

$$\frac{\partial}{\partial t}(\rho H) + \nabla \cdot (\rho \mathbf{v} H) = \frac{\partial p}{\partial t} + \mathbf{v} \cdot \nabla p - \nabla \cdot \mathbf{J}_H + \phi + S_H. \quad (2.10)$$

\mathbf{J}_H represents the heat diffusive flux² and S_H accounts for any additional volumetric source term of enthalpy.

Enthalpy H is defined in terms of the specific enthalpy H_α of each species α , as follows:

$$H = \sum_{\alpha=1}^{N_\alpha} Y_\alpha H_\alpha, \quad (2.11)$$

$$H_\alpha = H_\alpha^0 + \int_{T_0}^T C_{p,\alpha}(T) dT, \quad (2.12)$$

where $C_{p,\alpha}$ is the specific heat at constant pressure of species α and H_α^0 the specific enthalpy of formation at the reference temperature, T_0 .

Pressure terms in Eq. 2.10 can be neglected in the context of this project because they are only relevant when large pressure gradients are present (*e.g.* detonation problems) [28]. Besides, the term ϕ represents the viscous dissipation and can also be neglected for small Eckert numbers² [28]. Hence, Eq. 2.10 is simplified as follows:

$$\frac{\partial}{\partial t}(\rho H) + \nabla \cdot (\rho \mathbf{v} H) = -\nabla \cdot \mathbf{J}_H + S_H. \quad (2.13)$$

²More information in Appendix A.

2.2 Turbulence modeling

The above equations cannot be solved directly for most engineering applications. For Reynolds numbers typically present in real cases, these equations have very chaotic turbulent solutions, and it is necessary to model the influence of the smaller scales. Field properties become random functions of space and time that need to be averaged by expressing them as the sum of mean and fluctuating parts. The most commonly used method to treat turbulent flows is the Reynolds averaging method. However, in variable density flows, it is advantageous to use mass weighted averages, also known as Favre averaging [12].

In Favre averaging, for a generic field variable φ ,

$$\varphi \equiv \tilde{\varphi} + \varphi', \quad \tilde{\varphi} \equiv \frac{\int_T \rho(t) \varphi(t) dt}{\int_T \rho(t) dt} = \overline{\rho \varphi}, \quad (2.14)$$

where φ' is the perturbation part, whose effect is added to the mean part, $\tilde{\varphi}$.

Averaging the conservation equations leads to a set of new unknown quantities in the averaged equations; but no additional equations. Therefore, the system is an open system which needs to be closed with a set of equations to solve the unknowns. This establishes the central problem in turbulent flow analysis, known as the *closure problem*. At this point, the turbulence models arises as a procedure to close the mean flow equations. In Favre averaging, the most commonly used model for variable density flows is the $k - \varepsilon$ model.

2.3 $k - \varepsilon$ model

This model is the most widely used for turbulence modeling and the chosen one for this project. Its popularity in the industrial flow and heat transfer simulations comes from its robustness and reasonable accuracy for a wide range of turbulent flows. It is a semi-empirical model, and the derivation of its equations relies on phenomenological considerations and empiricism.

The standard $k - \varepsilon$ is a model based on transport equations for the turbulence kinetic energy k and its dissipation rate ε . The last one is the variable that determines how much the turbulence is dissipated, whereas the first one (k), determines the energy in the turbulence. Transport equations of the model are

$$\frac{\partial}{\partial t}(\rho k) + \frac{\partial}{\partial x_i}(\rho k v_i) = \frac{\partial}{\partial x_j} \left[\left(\mu + \frac{\mu_t}{\sigma_k} \right) \frac{\partial k}{\partial x_j} \right] + G_k + G_b - \rho \varepsilon - Y_M + S_k, \quad (2.15)$$

$$\frac{\partial}{\partial t}(\rho \varepsilon) + \frac{\partial}{\partial x_i}(\rho \varepsilon v_i) = \frac{\partial}{\partial x_j} \left[\left(\mu + \frac{\mu_t}{\sigma_\varepsilon} \right) \frac{\partial \varepsilon}{\partial x_j} \right] + C_{1\varepsilon} \frac{\varepsilon}{k} (G_k + C_{3\varepsilon} G_b) - C_{2\varepsilon} \rho \frac{\varepsilon^2}{k} + S_\varepsilon. \quad (2.16)$$

In these equations, G_k and G_b represent the generation of turbulence kinetic energy due to the mean velocity gradients in the first case and due to buoyancy in the G_b case. Y_M is the contribution of fluctuating dilatation in compressible turbulence to the overall dissipation rate³. $C_{1\varepsilon}$, $C_{2\varepsilon}$ and $C_{3\varepsilon}$ are the closure coefficients of the model itself [26]; σ_k and σ_ε are the turbulent Prandtl numbers⁴, and S_k and S_ε are some possible existing sources. Finally, μ_t is the turbulent viscosity and it is calculated as follows, being C_μ a constant:

$$\mu_t = \rho C_\mu \frac{k^2}{\varepsilon}. \quad (2.17)$$

2.4 Aerated gas burners

A gas burner is a device which produces a controlled flame by mixing a fuel gas with an oxidizer such as the ambient air or supplied oxygen and allowing for ignition and combustion.

Depending on how and when the fuel and oxidant are mixed we can differentiate the *aerated flames*, in which the gases mix prior to combustion due to an entrainment of primary air; and the *non-aerated flames*, where there is no primary air and therefore the combustion takes place with oxygen from the surrounding atmosphere (the secondary air). We can also distinguish between partially aerated and fully aerated flames (Figure 2.1).

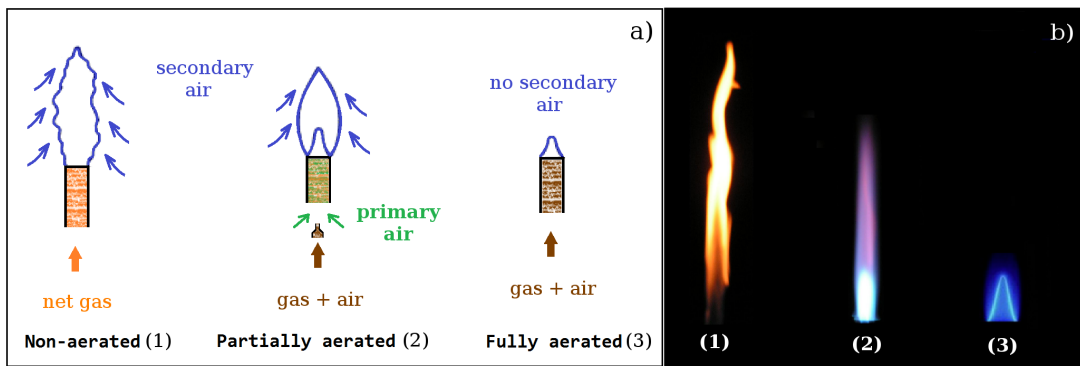


Figure 2.1 – Classification of flames according to the reactant feeding.

The main objectives when a burner is designed are the following:

- Ensure the correct mixture of gas and air.

³These three quantities are calculated as described in [5].

⁴More information in Appendix A.

- Have a controlled and reliable ignition.
- Guarantee the stability and the structure of the flame.
- The appliance is inherently safe.

To achieve these objectives, an understanding of the general structure and chemistry of a flame is fundamental.

2.4.1 Structure and performance of domestic burners

The main parts in which the burner is divided are the following:

- The **injector**, through which an overpressured gas fuel emerges.
- The **mixing tube**, engaged to mix the fuel and air.
- The **base**.
- And the **lid-spreader**, whose work is basically to promote a proper flow of the mixture towards the burner ports (Figure 2.2.a).

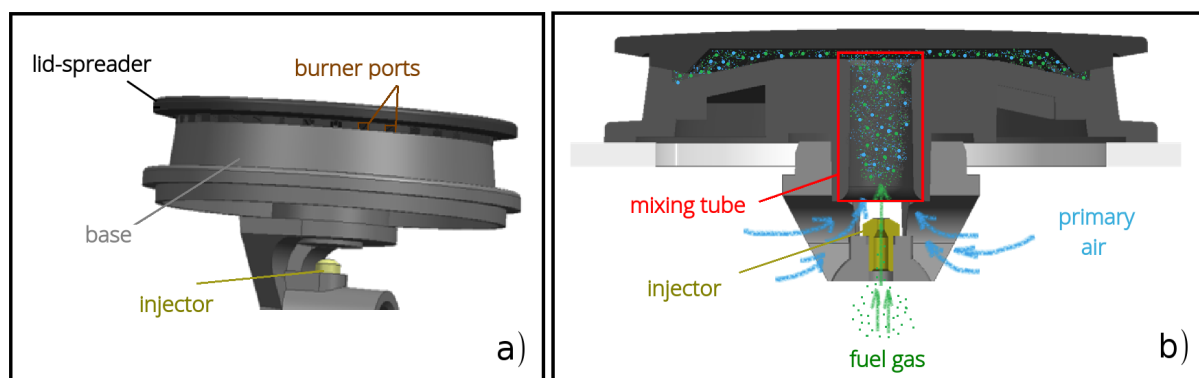


Figure 2.2 – a) Main parts of a domestic burner and **b)** the basic scheme of the burner interior.

Once the fuel gas is leaving the injector, it joins with the primary air by a momentum-sharing process between the gas and the ambient air. The gas mixture is produced through the mixing tube (Figure 2.2.b), which may be shaped as a Venturi tube. Then, the mixture impacts the lid and is redirected through the spreader to the burner ports. So far there is no combustion in the process; a spark is needed to start the reaction when the amount of air and fuel is within the flammability limits.

2.5 Flow passing an injector

Injectors are one of the fundamental components of a burner and must be carefully designed to ensure the correct supply of gas and air to the burner. In this section we will summaries the fundamental concepts and practical aspects of nozzle design.

In physical terms, an injector is a device that converts the potential energy from an overpressured gas supply into the kinetic energy of an emerging gas jet. In Figure 2.3 we can clearly appreciate, by simulation, how the gauge gas pressure⁵ drops to zero as the gas velocity increases rapidly and forms a high-velocity stream.

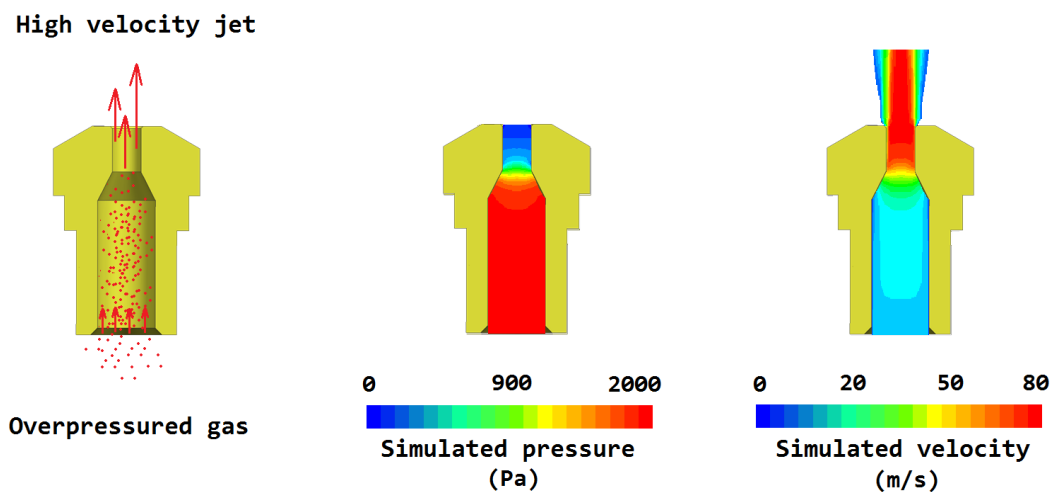


Figure 2.3 – Images from an injector simulation in which it can be observed the transformation of the potential energy of the gas into the high-velocity jet kinetic energy.

Namely, considering an injector without friction losses in the walls, energy conservation states that

$$g h_g = \frac{1}{2} v^2, \quad \text{or,} \quad \dot{V} = A_i \sqrt{2 g h_g}, \quad (2.18)$$

where \dot{V} is the volume flow rate from the orifice ($\dot{V} = v \cdot A_i$), A_i is the orifice area and h_g is the height of a column of gas required to exert the gas pressure at the orifice.

Above equation can be written in terms of the gauge pressure (p_g in mbar), the Wobbe number⁶ W (in MJm^{-3}) and the relative gas density (σ) in more conventional units (\dot{V} in $m^3 s^{-1}$, A_i in mm^2) as follows [20]:

$$\dot{V} = 1.278 \cdot 10^{-5} A_i W \sqrt{\frac{p_g}{\sigma}}. \quad (2.19)$$

⁵The Gauge pressure is the difference between the total pressure p , and the atmospheric pressure p_{atm} , so that $p_g = p - p_{atm}$. Therefore, a null gauge pressure is equivalent to the atmospheric pressure.

⁶More information in Appendix A.

The power rate is $q = Cv \dot{V}$, where Cv is the gas calorific value, so the theoretical power rate from the orifice (in watts) is given by Eq. 2.20. This constitutes a basic discharge flow equation from an orifice

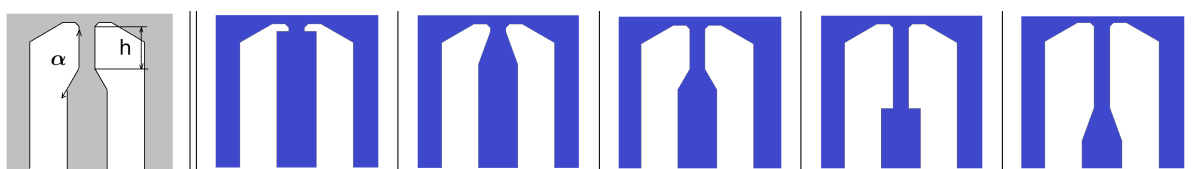
$$q = 12.78 A_i W \sqrt{p_g}. \quad (2.20)$$

2.5.1 Coefficient of discharge

In practice, the flow passing an orifice is reduced due to friction losses and Eq. 2.20 needs to be corrected by a factor usually called *discharge coefficient Cd*:

$$q = 12.78 A_i W Cd \sqrt{p_g}. \quad (2.21)$$

The discharge coefficient varies between zero and one. A coefficient equal to one means that there are no losses and that the injector power rate is equal to that of the ideal case (Eq. 2.20), and a zero coefficient implies that all flux is lost due to friction.



h (mm)	0.25	0.25	2.5	5	5
α (°)	90	160	150	90	160
Cd	0.71	0.88	0.84	0.73	0.79

Table 2.1 – Different examples of injector geometries and their respective discharge coefficients. The third geometry is a typical configuration for a commercial injector. Geometries and discharge coefficients are part of the results of this project.

The orifice shape and the Reynolds number⁶ are the two main parameters on which the discharge coefficient depends. Generally speaking, dependence on shape indicates that if the height of the orifice tube (h) is too long compared to the diameter of the injector, the energy loss due to friction is high; and if the tube is too short, energy is lost by the sudden contraction and expansion of the gas. On the other hand, the discharge coefficient depends on the Reynolds number defined by $Re = \frac{v_0 l_0}{\nu}$. The characteristic length l_0 in an injector is the orifice diameter, hence the relation between discharge coefficient and Reynolds number is Eq. 2.21. For a typical orifice with laminar flow, the discharge coefficient is strongly dependent on Re , while for fully turbulent flows the dependence is considerably lower and practically constant for the same orifice diameter.

2.6 Air entrainment

This is another fundamental aspect for burner designers. The amount of primary air has a considerable effect on some important flame variables, such as stability, shape and temperature, for example.

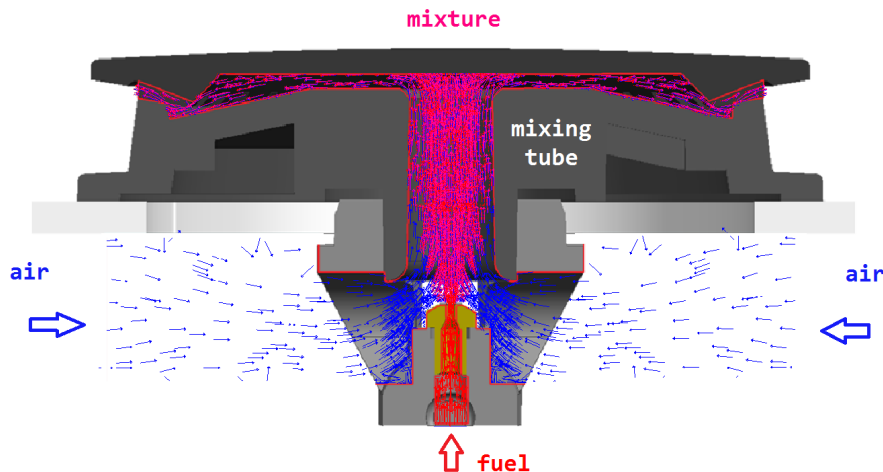


Figure 2.4 – Air-fuel mixture entrainment in a burner.

Figure 2.4 shows the basic air entrainment mechanism. The over-pressured gas emerges as a free stream from the orifice at a rate that depends on pressure itself, orifice dimensions and the composition of the gas. Momentum transfer occurs between the jet and the surrounding air, resulting in entraining and expanding process at the inlet of the mixing tube. Owing to turbulence, it is common to assume that the mixing is complete before it impacts into the lid, producing a decrease in momentum and velocity and a slight increase in pressure; redirecting the gas to the burner ports.

2.6.1 Aeration

Directly related with the air entrainment there is an important variable to take into account in our study, the Air-Fuel Ratio, AFR. The AFR is just the ratio between the mass air and the mass of fuel in a combustion process:

$$AFR = \frac{m_{air}}{m_{gas}} = \frac{m_{O_2} + m_{N_2}}{m_{gas}}. \quad (2.22)$$

If there is an excess of fuel in the mixture, it is called a *fuel-rich* mixture. On the contrary, if there is an excess of oxygen, it is called a *fuel-lean* mixture. Finally, if exactly enough air is provided to completely burn all of the fuel, the mixture is called *stoichiometric*⁷ (Figure 2.5).

⁷Often and hereafter abbreviated to *stoich*.

For the stoich case, the AFR is known as the stoichiometric mixture ratio (or stoich ratio). Different fuels have different stoich ratios because some require more air than others to achieve a complete combustion. Having different stoich ratios for each fuel is a nuisance that can be avoided if we work with the *aeration lambda*, λ . The advantage of working in lambda is that regardless of the fuel we were using, the stoichiometric is always the same value, one.

There is a direct relation between λ and AFR:

$$\lambda = \frac{AFR}{AFR_{stoich}}, \quad \text{and for methane} \quad \lambda = \frac{1}{17.167} \frac{m_{O_2} + m_{N_2}}{m_{CH_4}}. \quad (2.23)$$

As we mentioned before, $\lambda = 1$ means a stoichiometric mixture. For $\lambda < 1$ the mixture is rich, and $\lambda > 1$ means a lean mixture (Figure 2.5).

We can see that the greater the quantity of fuel, the lesser the value of lambda and vice versa. Typical values for lambda in an air-fuel mixture arriving to a burner port oscillate between 0.4 and 0.7. The ideal situation would be to achieve the largest and possible value of lambda for a given injector power, without compromising the flame stability. Next equation is the relation between the injector power rate and the fuel mass flow rate

$$q = \dot{m}_{fuel} h_s, \quad (2.24)$$

where \dot{m}_{fuel} is the mass flow rate of the gas in the injector entrance and h_s is the heat of combustion of methane, $h_s = 55.68 \text{ MJ/kg}$. Eq. 2.24 means that an increase in the fuel mass, and therefore in fuel mass flow rate, would imply an increase in injector power rate. Therefore, the challenge is to maximize the aeration along with the injector power.

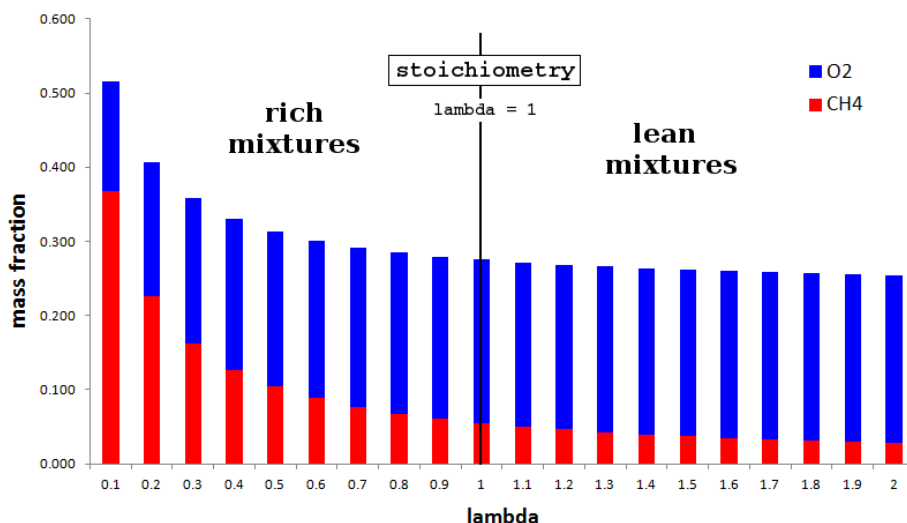


Figure 2.5 – Mass fractions of fuel (red) and oxygen (blue) corresponding to their lambda value represented for methane.

Chapter 3

Optimization Theory

*Nothing takes place in the world whose meaning is not that
of some maximum or minimum.*

Leonhard Euler

3.1 Introduction to Design Exploration

Design Exploration is a process used to investigate and evolve the design space intending to discover the optimal design and informing of decision making throughout the design process. The main purpose of Design Exploration is to identify the relationship between the performance of the product and the design variables. Based on the results, you can identify the key parameters of the design and how they affect product performance. With this knowledge, it is possible to influence the design so it meets the product requirements.

Following the Design Exploration process, particularly using DOE tool and response surfaces, it is possible to get the relationship between some design variables and the performance of the study case. The first step in the process is to create a simulation model and then define the parameters to investigate. Based on the information you enter in the DOEs, the response surface system creates the design space sampling, which also depends on the selected DOE type. When you perform the DOE, a response surface is created for each output parameter. After the DOEs are simulated and response surfaces are created, the next step is analyzing the results with a correlation analysis using curves, surfaces, and sensitivities for example. As soon as

you have explored the design and understand correlations and sensitivities, the following step is to optimize the design to meet the required constraints. Finally, a probabilistic analysis can quantify the reliability or quality of the product statistically.

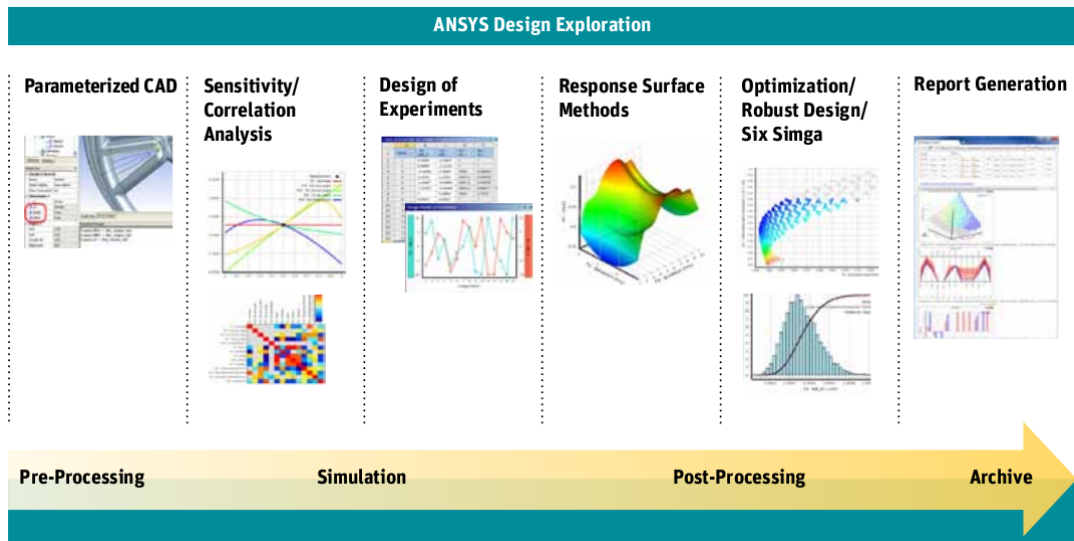


Figure 3.1 – ANSYS Design Exploration process.

The ANSYS tool for the Design Exploration (DesignXplorer) follows the workflow described above (see Figure 3.1).

3.2 Design Of Experiments (DOE)

DOE is a technique used to guide the choice of experiments to be performed efficiently. Within the theory of optimization, an experiment is a series of tests in which the input variables are changed according to a rule to identify the reasons for the changes in the output response. There is a wide range of DOE algorithms or methods available in engineering literature. However, they all have common characteristics. They try to locate sampling points such that the space of random input parameters is explored in the most efficient way, or they try to get the required information with a minimum of points. Sample points in efficient locations not only reduce the required number of design points but also increase the accuracy of the response surface.

3.2.1 Terminology

To perform a DOE, it is necessary to define the problem and choose the variables, which are called the *factors* or parameters. A *design space* or *sampling space* must be defined, *i.e.*, a range of variability must be set for each variable. The number of values that the variables can

assume in DOE is restricted and small. The DOE technique and the number of levels have to be selected according to the number of experiments which can be afforded. By the term *levels* we mean the number of different values in which a parameter is discretized, that is usually the same for all. In the sampling space are placed the *Design Points* (DP), or *sampling points*, which represent every single simulation to be run, *i.e.* each experiment with different nozzle configuration.

3.2.2 DOE Types

Depending on how the points are sampled in the working space, we can consider two types of DOEs. In the first type there is a random choice of the points using a *space filling* technique, and in the second one, the collocation of points depends on the levels and factors, and they are called *full factorial* DOEs.

The full factorial is probably the most common and intuitive strategy of experimental design. The samples are given by every combination of the parameters values. Therefore, the sample size is $\prod_i L_i$, being L_i the number of levels for each parameter. As the sample size grows exponentially with the number of factors, sometimes it is necessary to use a *fractional factorial* design to reduce the total time. The fractional factorial design consists of running only a subset of the full factorial experiments. By doing so, it is still possible to provide good information about the main effects and some information about interaction effects.

The space filling DOE techniques rely on different methods for filling uniformly the design space. Therefore, they are not based on the concept of levels and do not require discretized parameters. The most obvious space filling technique is the random one, by which the design space is filled with uniformly distributed, randomly created samples. Space-filling techniques are a good choice for creating response surfaces, although the randomness can produce the clustering of some samples, resulting in a lack of effectiveness.

Within each DOE type, there are more classifications according to the way of filling the sampling space and the number of design points. Three DOE types present in the ANSYS DesignXplorer will be explained. The first belongs to the full-factorial family, the Central Composite Design. The second is an example of the space filling group, namely, the Optimal Space Filling. And the last one is the custom DOE, in which the sampling points are collocated as the user decides.

Central Composite Design (CCD)

This DOE type is a five-level fractional factorial design with the central point and the star points added. Five-level means each factor will have five sample points in each direction of the space, represented by $(-p_i, -1, 0, 1, p_i)$, where $(-1, 1)$ corresponds to the physical lower and upper limits of the explored range. The value of p_i varies depending on the design property and the number of factors in the study. For example, in two dimensions the total number of points is nine, and there is an enhanced version with seventeen (Figure 4.4). The CCD design is the most used option and the recommended one in the ANSYS software.

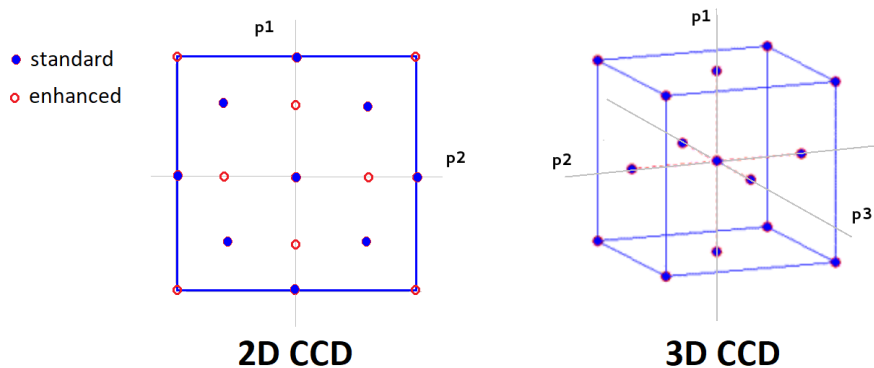


Figure 3.2 – Sampling space configurations for 2D and 3D CCD designs. Red points represent the enhanced version.

Optimal Space Filling (OSF)

This is an advanced form of the Monte Carlo sampling method. In OSF the points are randomly generated in a square grid across the design space, avoiding the clustering of samples (Figure 3.3). Two points do not share the same value, *i.e.* no two points share a row or a column of the grid with another point. The distance between points is maximized through several iterations to achieve a more uniform distribution. The main disadvantage of this method is the poor coverage of extremes. OSF aims to conserve optimization resources by avoiding the duplication of points and result in a high-quality response prediction with an adequate number of DP.

Custom

With a Custom DOE, design points can be manually added to the design points table by introducing the parameters and the desired levels into which they will be divided. Using this DOE, the sampling space can be filled efficiently. For example, if our problem only needs to cover corners and a small area of space, this is the right DOE to use. Or, if it is necessary to improve one of the previous DOEs by adding new points, this would be the way.

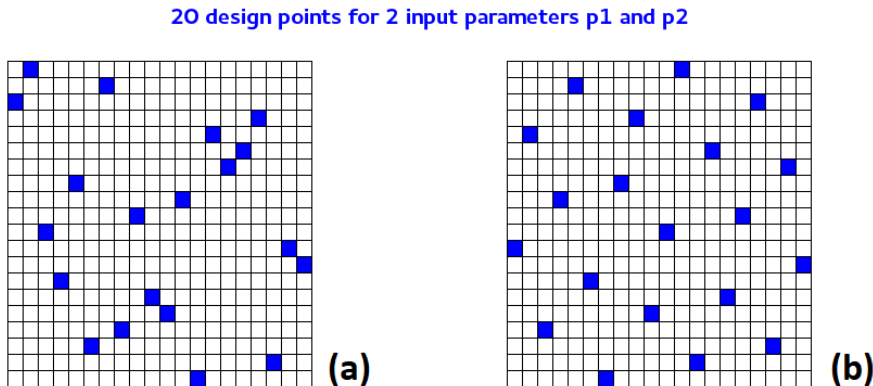


Figure 3.3 – 2D OSF sampling space, before (a) and after (b) maximizing the distance between points.

3.3 Response Surface

Response Surfaces (RS) are functions in which the output parameters are described in terms of the input parameters. The main idea is to use the results of a DOE to create an approximation of the response variable over the design space. The reason for building an RS is that, although it is just an approximation, it can estimate the set of input parameters yielding an optimal response. The RS is an analytical function, thus the optimization process is quick and does not require additional experiments or simulations to be performed.

From a mathematical point of view, the objective function, or response variable, r , is an unknown function of the input parameters p_i . The response surface \hat{r} is an approximation of this function and it is expressed as follows:

$$r = f(p_i) = \hat{f}(p_i) + \epsilon(p_i) \implies \hat{r} = \hat{f}(p_i), \quad (3.1)$$

where $\epsilon(p_i)$ is the estimation error.

The results of a DOE made of N simulations or experiments consists of $N(p_{ij}, r_j)$ couples in which a point p_{ij} of the design space is associated with the response value r_j . If $r_j = \hat{f}(p_{ij})$ holds for each sample point, the RS is said to be an *interpolating* response, or an *approximating* response if the estimating error is not zero, $\epsilon(p_i) \neq 0$.

3.3.1 Response Surface Techniques

The first use of response surfaces was in 1951 [10] and the proposal was to use a first-degree polynomial model for approximating a response variable. Since then, many techniques have been developed, each one with varying characteristics that leads to different responses. The

choices of responses in ANSYS software are: Genetic Aggregation, Standard Response Surface - Full 2nd-Order, Kriging, Non-Parametric Regression and Neural Networks.

Genetic Aggregation

This is the default algorithm in ANSYS DesignXplorer and the chosen one to use in this project. Automatically, it selects and configures the RS best suited to each output in your system, choosing among the other ones. This algorithm is more reliable than the classical response surfaces, and the natural choice, even although it takes more time for solving than the rest.

Genetic Aggregation uses a genetic algorithm that generates populations of the different RS and selects which one yields the best approach. It considers the accuracy of the RS as well as its stability. To get the most effective RS, the algorithm generates a population of meta-models with different types and settings. Each RS quality is assessed using a Cross-Validation (Leave-One-Out and K-Fold) and the best ones are selected for reproduction. If one of them meets the quality requirements, or if the algorithm has reached the maximum number of iterations, the algorithm stops. The next populations are obtained by cross-over and mutation of the previous population by randomly changing a RS setting (a gene of the algorithm)(see Figure 3.4).

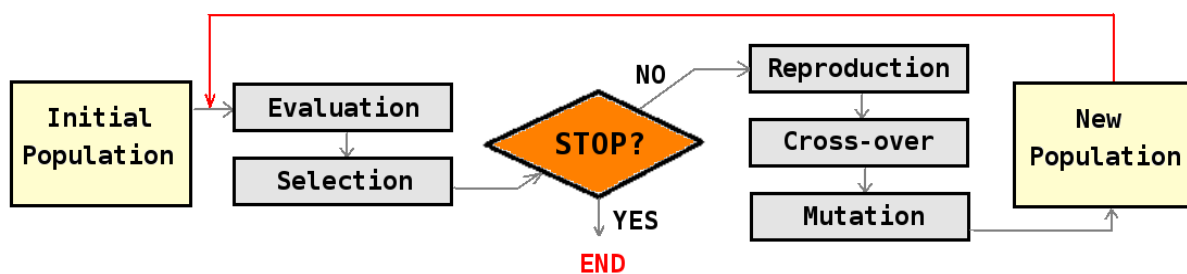


Figure 3.4 – Genetic Aggregation algorithm.

The Genetic Aggregation has the possibility of auto refinement, which generates design points until response surface accuracy meets the user requirements. The goal is to accomplish the three main criteria: accuracy, reliability, and smoothness.

Standard Response Surface

This RS is based on a modified quadratic formulation, *i.e.* \hat{f} is a second order polynomial approximation. It provides satisfactory results if the output parameter variation is smooth (Figure 3.5).

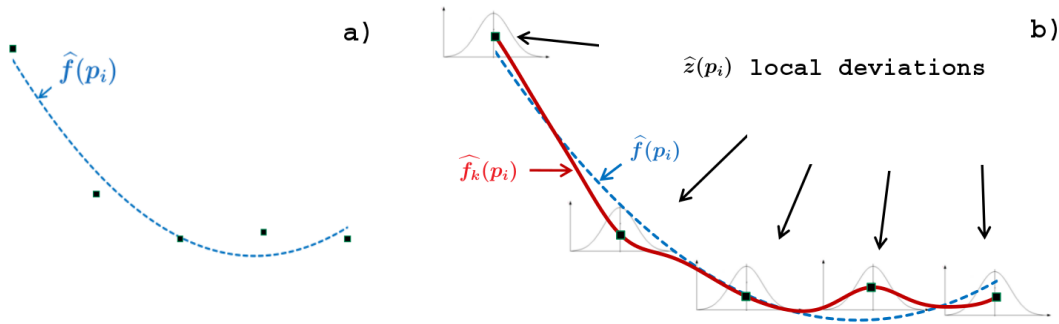


Figure 3.5 – Standard response surface (a) and Kriging (b) approximations. *Source: [4]*

Kriging

The Kriging RS is a multidimensional interpolation combining a polynomial model which provides the global behavior of the RS, plus a perturbation term, which dictates the local behavior around the response points (Figure 3.5). It provides a better approximation than the Standard RS when the output response is highly nonlinear. It is efficient in numerous cases, but not for those with noisy results.

Non-parametric Regression

This approximation belongs to a general class of Support Vector Method type techniques [27]. The idea is to build a RS with a margin of tolerance by creating a narrow envelope around the true output surface (Figure 3.6). It is adequate when the results are noisy and the responses nonlinear.

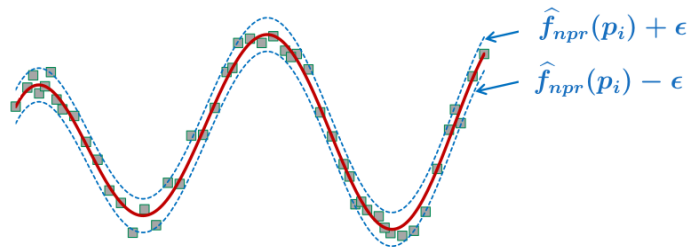


Figure 3.6 – Non-parametric Regression. *Source: [4]*

Neural Network

Here, the RS is built with a neural network of three levels, one for the input parameters, other for the outputs and the last one is the hidden layer of the network (Figure 3.7). Each connection between levels is associated with a weight function, send out from an algorithm that minimizes in each iteration the distance between interpolation and the design points (the so-called learning

process). It is suited for nonlinear, noisy responses.

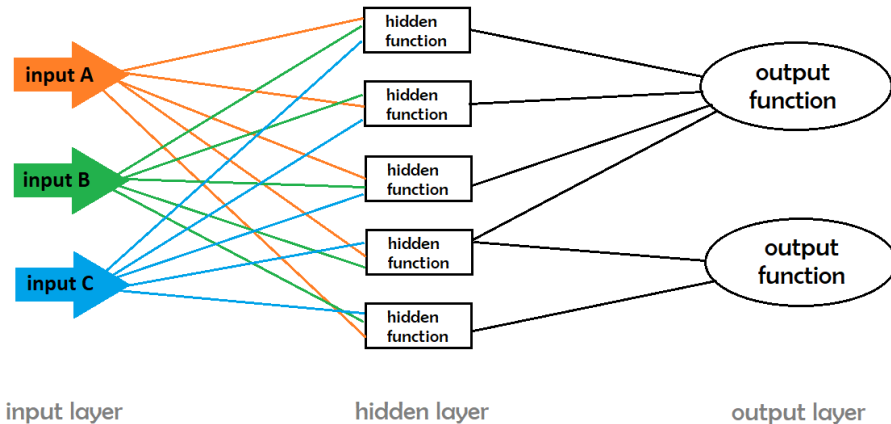


Figure 3.7 – General scheme of a neural network response surface with one hidden layer.

Source: [4]

3.3.2 Refinement Points

These are points added to the model to enrich and improve the response surface. As with design points, DesignXplorer must perform a design point update (a real solve, a new simulation) to get the output parameters for the refinement points. The refinement points are used to build the response surface and are taken into account for the generation of verification points. Along with DOE points, refinement points are used as *learning points* for quality calculations.

3.4 Quality Metrics

DesignXplorer software uses two main criteria, the Goodness of Fit and Verification Points. Used together, they enable to asses and improve the quality of the response surface.

3.4.1 Goodness of Fit (GOF)

Response surfaces are built from the design points in the DOE and refinement points if any, which are altogether called *Learning Points*. Goodness of Fit metrics compares the RS outputs with the DOE results used to create the response itself.

The statistical metrics that ANSYS uses in Goodness of Fit calculations are the following:

Coefficient of Determination

The Coefficient of Determination R^2 is the proportion between the variance in the output parameter, that can be explained by RS regression equation, and the total variation:

$$R^2 = 1 - \frac{\sum_{j=1}^N (r_j - \tilde{r}_j)^2}{\sum_{j=1}^N (r_j - \bar{r})^2},$$

where:

- r_j is the value of the output parameter in the j-th sampling point,
- \tilde{r}_j is the value of the regression model at the j-th sampling point,
- \bar{r} is the arithmetic mean of the values of r_j ,
- N is the number of sampling points.

The points used to create the response surface are likely to contain variation for each output parameter unless the RS is interpolating. In such a case, as Kriging RS, the R^2 would be 1, but without meaning a high-quality RS.

Root Mean Square Error (RMSE)

RMSE is the square root of the average square of the DOE residuals:

$$\text{RMSE} = \sqrt{\frac{1}{N} \sum_{j=1}^N (r_j - \tilde{r}_j)^2}.$$

Relative Maximum Absolute Error (RMAE)

This criterion stands for the absolute maximum residual value relative to the standard deviation of the actual output data:

$$\text{RMAE} = \frac{1}{\sigma_r} \max_{j=1:N} |r_j - \tilde{r}_j|,$$

where σ_r is the standard deviation of r_j values.

Relative Average Absolute Error (RAAE)

This criterion is the average of the residuals relative to the standard deviation

$$\text{RAAE} = \frac{1}{N \sigma_r} \sum_{j=1}^N |r_j - \tilde{r}_j|.$$

Goodness of Fit is closely related to the response surface type used to generate the response surface. For approximating responses (such as Standard Response Surface), this criterion indicates how well the fit was accomplished. However, for interpolated responses in which the RS is forced to pass through all the DOE points (such as Kriging), these criteria do not show whether the response surface captures the parametric solution. Therefore, if the quality of the response

is not the expected one, an option to improve it would be to change the response surface type. However, with Genetic Aggregation (our case), this problem is not present because the GOF metrics are also calculated for learning points but via the cross-validation technique (K-Fold and Leave-One-Out methods). That technique provides an especially effective way to assess the stability of the response. If the GOF metrics for cross-validation learning points are good, you can be confident in the quality of your model. If these GOF metrics are not good enough, you know you need to enrich your model by adding new refinement points.

3.4.2 Verification Points (VP)

This is another tool that enables verifying the accuracy of the RS. They are points that compare the predicted and observed values of output parameters. Each VP is a new experiment (new design point) simulated from scratch and it is later compared with the value predicted from the RS. Verification points are subsequent to the calculation of the RS and therefore, they are not used to build it. If a verification point reveals that the current RS is of poor quality, you can insert it as a refinement point to improve the accuracy of the RS.

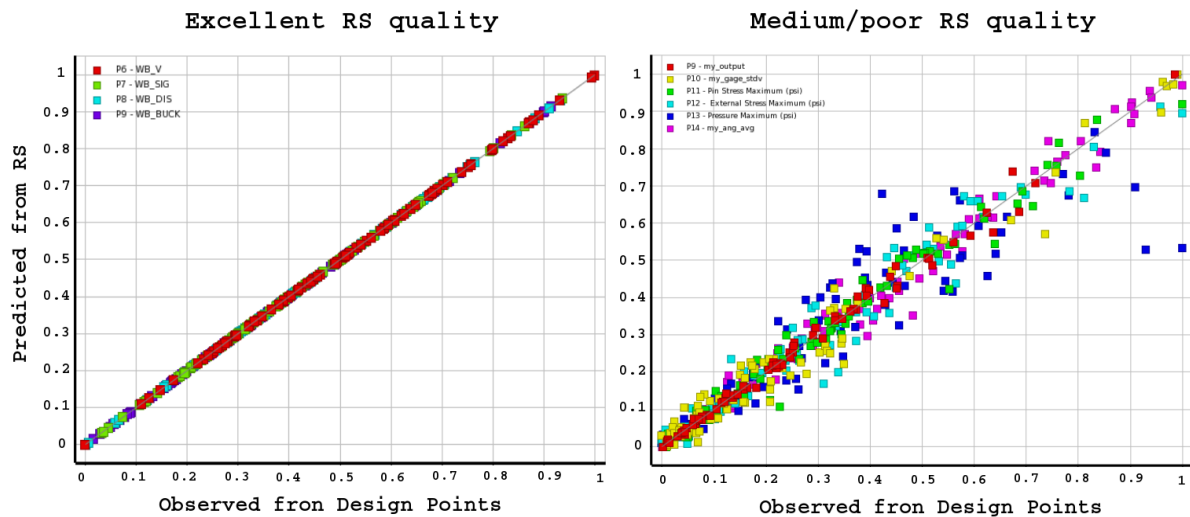


Figure 3.8 – Goodness of Fit chart examples. *Source: [4]*

In Figure 3.8 there is an example of VP-charts that represent two different-quality responses. They show the values predicted from the response surface versus the values observed from the design points or versus the verification points. This kind of figures helps to identify if the response surface correctly fits the points of the design points table and refinement table. The closer the points are to the diagonal line, the better the response surface fits the points.

In conclusion, the goodness of fit criteria, when calculated for different points, measure different aspects of the RS. For learning points (design points + refinement points), the criteria show

the quality of the RS interpolation; and for VP it is the quality of the prediction which is being measured.

3.5 Optimization

Once we have explored the design and understood correlations between input and output parameters, the following step may be to optimize the design. In this work, the tool DesignXplorer includes several algorithms that help to identify the most suitable candidates, taking into account multiple objectives and performance trade-offs. DesignXplorer offers two types of optimization procedures, the *Response Surface Optimization* and *Direct Optimization*. With the Direct Optimization is not needed the calculus of the responses surfaces or DOEs and the process can be started just by having the sampling space.

The Response Surface Optimization (RSO) is based on a DOE and draws its information from the RS; hence it depends on the RS quality. The computational time of this optimization is almost costless; the time is spent in the DOE step. Optimal results are approximated since the algorithms use RS evaluation rather than solution from new simulations.

On the other hand, Direct Optimization (DO) works with real solutions (new simulations) instead with evaluations of the RS. As a result, changing the optimization criteria and re-running is highly computationally time-consuming. Here, the optimal results rely on actual resolution. This optimization is suitable for cases where the computational time of each case is small and there is no interest in controlling the spatial distribution of design points or response surfaces. Our case does not fit within these criteria, so we will use the Response Surface Optimization procedure.

The methods for Response Surface Optimization available in ANSYS software are Screening, Multi-Objective Genetic Algorithm (MOGA), Nonlinear Programming by Quadratic Lagrangian (NLPQL) and Mixed-Integer Sequential Quadratic Programming (MISQP) [3,11].

Within these methods, those with the capability of dealing with only one objective are NLPQL and MISQP. They are gradient-based optimization methods for constrained problems. The NLPQL is based on quasi-Newton methods and MISQP solves mixed-integer non-linear programming by a modified sequential quadratic programming method.

The multi-objective methods are Screening and MOGA. Screening is a direct sampling method that uses a quasi-random number generator based on the Hammersley algorithm. However,

	Single objective	Multi Objective	Local search	Global search	Discrete values
NLPQL	✓		✓		
MISQP	✓		✓		✓
Screening		✓		✓	✓
MOGA		✓		✓	✓

Table 3.1 – Capabilities of the Response Surface Optimization methods available in ANSYS software. *Source: [3]*

MOGA is an iterative method that uses a genetic algorithm to optimize problems with continuous input parameters. Table 3.1 summarizes the main aspects to consider when choosing one method or another. Further information can be found in [3, 11].

The choice of the optimization method depends on the properties of each case. In this project, a multi-objective optimization method is needed, and the only two capable of handling over one target are the Screening and MOGA methods. Screening is typically used to find a first set of candidate points for a preliminary design. Then, if a refinement is required, these points are used as starting points for other optimization methods.

Therefore, in this project the MOGA method will be the selected for performing the optimization, using the Screening points to start MOGA. MOGA can be used for both Response Surface Optimization and Direct Optimization. It is available for many types of input parameters and uses a genetic algorithm to generate the initial samples. Then, using cross-over and mutation for the next populations, it iteratively searches for the feasible points for creating the Pareto front.

The Pareto Front

In multi-objective optimization, there is rarely a feasible solution that minimizes or maximizes all objective functions simultaneously. In this situation, there is typically a group of solutions called *Pareto optimal solutions* [23]. They are solutions that cannot be improved in any of the objectives without deteriorating at least one other. There is usually an infinite number of Pareto optimal solutions, and they are usually referred to as the *Pareto front*.

Chapter 4

Case configuration

We build too many walls and not enough bridges.

Isaac Newton

Previous chapters of this project describe the theoretical concepts involved in the process of optimizing the injectors geometry to achieve maximization requirements. In this chapter, we present the case and setup details. In the first part, the configuration of the case will be exposed, describing the geometry, the boundary conditions and the mesh. And in the last part, the DOE configurations used in the project are also presented, showing the exact placement of design points in the sampling space.

4.1 Description of the case

The study case of this project comprises a gas burner injector through which an over-pressured gas enters, creating a high-velocity jet in the outlet that entrains the surrounding free air. It is a three-dimensional case although it can be simulated in two dimensions assuming an axial symmetry, capturing the most essential features on the flow using a reduced computational load.

4.1.1 Geometry

In Figure 4.1 it is shown the modeling of the injector, starting with the solid parts, then defining the fluid zone and obtaining the 2D fluid domain.

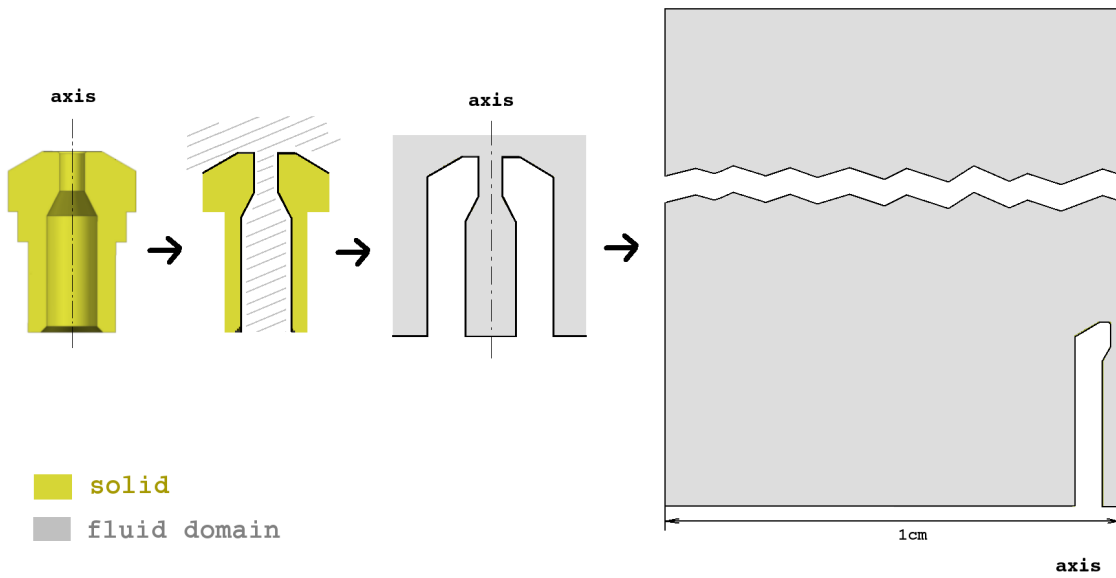


Figure 4.1 – Fluid-domain modeling for the injector of gas of our case.

In a closer view of the injector zone (see Figure 4.2), the two geometrical parameters of the injector used for this study can be seen. Namely, the height, h , of the injector throat⁸, and the angle, α . The range of variation of the parameters is $h \in [0.25, 5]$ (mm), and $\alpha \in [90, 160]$ ($^{\circ}$). Therefore, the sampling space in our case is the rectangle $SP = [0.25, 5] \times [90, 160]$ (Figure 4.2). The variation ranges have been chosen to consider the dimensions of the base case and potential manufacturing constraints. The height, angle and diameter for the base case are $h_b = 1.8$ mm, $\alpha_b = 153^{\circ}$ and $D_b = 1$ mm respectively.

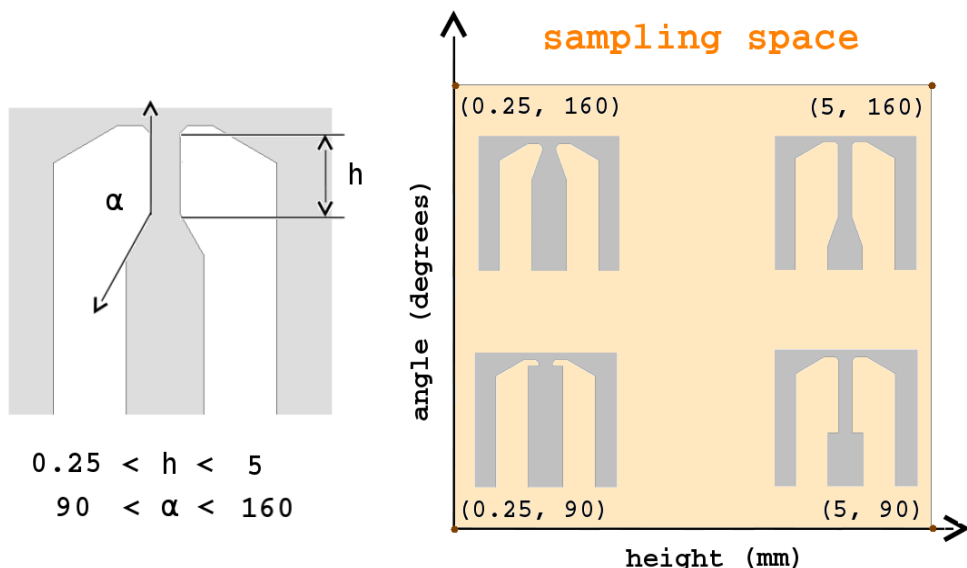


Figure 4.2 – Geometrical parameters h and α and the sampling space with the four extreme geometries corresponding to the space corners.

⁸The narrowest internal part of the injector

As an example of design points, in the right part of the Figure 4.2, there are four injector geometries corresponding to the corner design points. The two configurations at the bottom correspond to the minimum angle and heights of the extremes, and vice versa for the two geometries at the upper part.

4.1.2 Boundary conditions

The case consists of two inlets and one outlet with a fixed pressure condition, the revolution axis and one standard wall set as slip-symmetry wall (Figure 4.3).

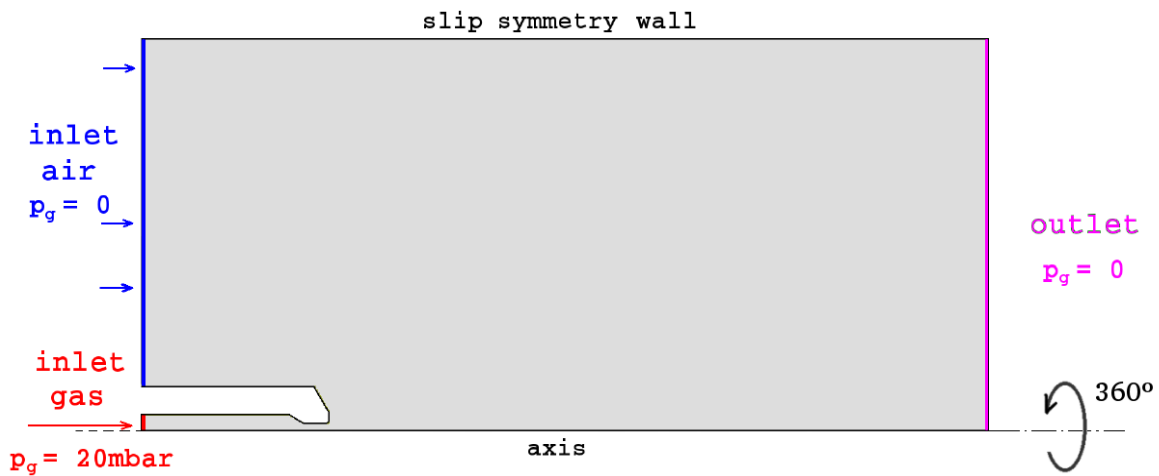


Figure 4.3 – Boundary conditions of the case.

Both the inlet of air and the outlet are set to a zero gauge pressure, which is equivalent to work under the atmospheric pressure. However, the gas passing through the injector is over-pressured with 20 mbar for methane. This quantity is regulated by the European Standard [17]. Besides, the configuration has axial symmetry with respect to the bottom axis and finally, the upper wall is set as a symmetry wall. This last condition is located far enough from the axis so that the injector and the jet do not suffer its effect.

4.1.3 Mesh

This is an essential part of all simulation processes. It affects such important aspects as the convergence, the quality of the results and/or the total computational time, for example. A study of the influence of the mesh will determine the appropriate one for this case. However, the main aspect to consider for this project is that there is not a single case. A very large number of simulations are needed to carry out the complete study of DOEs and Direct Optimization, hence mesh requirements and computational time for every single run has to be adequate.

	Coarsened Case	Base Case	Refined Case
mesh elements size (mm)			
injector mesh detail			
cells	58896	225152	996787
skewness	0.662	0.727	0.639

Table 4.1 – Numerical details of the three used meshes. It is shown the size of the mesh elements in each domain zone, the total number of elements as well as the maximum mesh skewness.

Based on previous experience with these configurations, an initial mesh has been created (base case in Table 4.1). Then, the number of elements of the mesh has been increased and decreased by approximately four times to obtain both a refined and a coarsened mesh. Finally, the three cases have been performed with the same settings and with the same convergence criteria. Four critical variables for the convergence have been chosen to compare the results and see how the mesh is affecting them, to wit:

- the **total mass flow rate** at the outlet (\dot{m}_{out}),
- the **gas mass flow rate** entering the injector (\dot{m}_{gas}),
- the **methane mass fraction** in the outlet (Y_{CH_4}),
- the outlet **gas velocity magnitude** (v_{out}).

Considering previous results (see Table 4.2), the base case seems to be an optimal mesh for this study. It takes a reasonable computing time for high-quality results, very similar to those of the refined mesh. The coarsen mesh also achieves good results compared with the refined one, and even in a lesser computational time. However, the number of cells that this mesh has in the narrowest part is not enough to capture properly the phenomena related to the expansion and later mixing as it is shown by differences in the concentration of Y_{CH_4} . Therefore, considering

	Coarsened Case	Base Case	Refined Case
CPU time/iter	0.522 s	1.751 s	12.695 s
\dot{m}_{out} (kg/s)	$4.101 \cdot 10^{-2}$	$4.112 \cdot 10^{-2}$	$4.111 \cdot 10^{-2}$
\dot{m}_{gas} (kg/s)	$5.282 \cdot 10^{-5}$	$5.404 \cdot 10^{-5}$	$5.384 \cdot 10^{-5}$
Y_{CH_4}	$1.280 \cdot 10^{-3}$	$1.316 \cdot 10^{-3}$	$1.310 \cdot 10^{-3}$
v_{out} (m/s)	1.153	1.159	1.162

Table 4.2 – Results obtained for the three cases. It is shown the computational time required per iteration, the total mass flow rate at the outlet \dot{m}_{out} , the mass flow rate of the gas in the inlet \dot{m}_{gas} , the mass fraction of methane in the outlet Y_{CH_4} , and the stream velocity also in the outlet v_{out} .

that the difference in CPU time and quality of results with the base case is small, and viewing the really good concordance between the base case and the refined one, we can conclude that the best choice is the base case mesh.

4.2 DOE configurations

All the DOE configurations to be performed are presented in this section (Figure 4.4). The idea is to compare the three main types of DOEs seen in Chapter 3. Namely, the factorial, the space-filling and the custom DOE configurations. By doing that, we can determine how the distribution of the points and the amount of them affect the results. The DOE with the best performance will be chosen for the main injectors study.

Two possible CCD configurations have been studied: the basic distribution with nine DP, and the enhanced one with seventeen (CCD9, CCD17). Therefore, to compare the results in similar conditions, the OSF has also been run with nine and seventeen sampling points (OSF9, OSF17). The ideal situation would be to have the custom DOE configurations also with nine and seventeen points. Thus, a good third possibility may be the full-factorial distribution with three and four levels, resulting in a nine and sixteen sampling points (CUS9, CUS16). The full-factorial collocates the points uniformly and equidistant along the axis.

Also, the number of points will be studied because sometimes seventeen could be a poor configuration. For example, when the sampling space is large enough or with abrupt discontinuities. Then, the custom and OSF DOEs will be studied with almost the double amount of points (CUS36, OSF36). Because of the custom DOE restriction, instead of exactly using the double

of runs (thirty-four), the sampling space has been divided into six parts and therefore a thirty-six-configuration has been used. The CCD is a five-level DOE and is not possible to run other configurations but those above mentioned.

Summing up, the DOE configurations to be studied are CCD9, CCD17, OSF9, OSF17, OSF36, CUS9, CUS16 and CUS36.

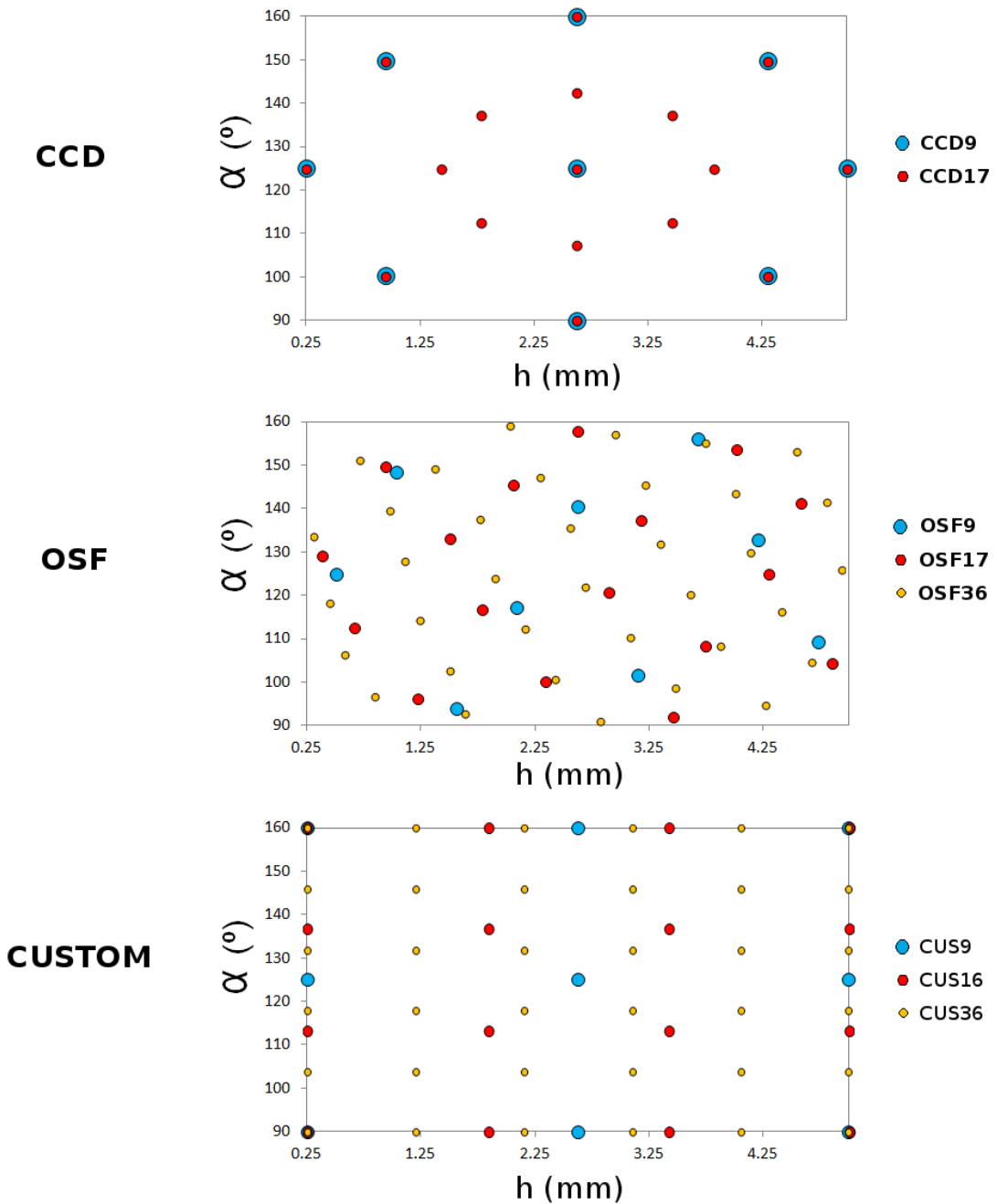


Figure 4.4 – Sampling space distributions of all tested DOEs.

Chapter 5

Results

*You wake me up early in the morning to tell me that I am right?
Please wait until I am wrong.*

John Von Neumann

Eight different DOEs (149 injector simulations) have been performed to determine the optimal configuration. Once the DOEs had finished, the genetic aggregation was used to build the response surfaces without refinement. Then, to decide the quality of DOE predictions, five verification points have been simulated and used, along with the DOE points, to calculate the quality criteria explained in Chapter 3.

Once the optimal DOE was chosen, an analysis of the output sensitivities regarding the input parameters was performed to see the influence of physical variables. In the next step, the response surfaces of most-affecting variables were refined to use them for analyzing the physics behind the problem. Finally, Response Surface Optimization procedure has been performed using the MOGA method to find candidates that optimize the aeration and the injector power rate at the same time for a fixed pressure.

5.1 DOE quality metrics

The graphs below represent the comparison between the value of the discharge coefficient and aeration of design points and the predicted values from the response surface. Also, VP have been simulated to measure the quality of DOE predictions and are also represented in the graphs.

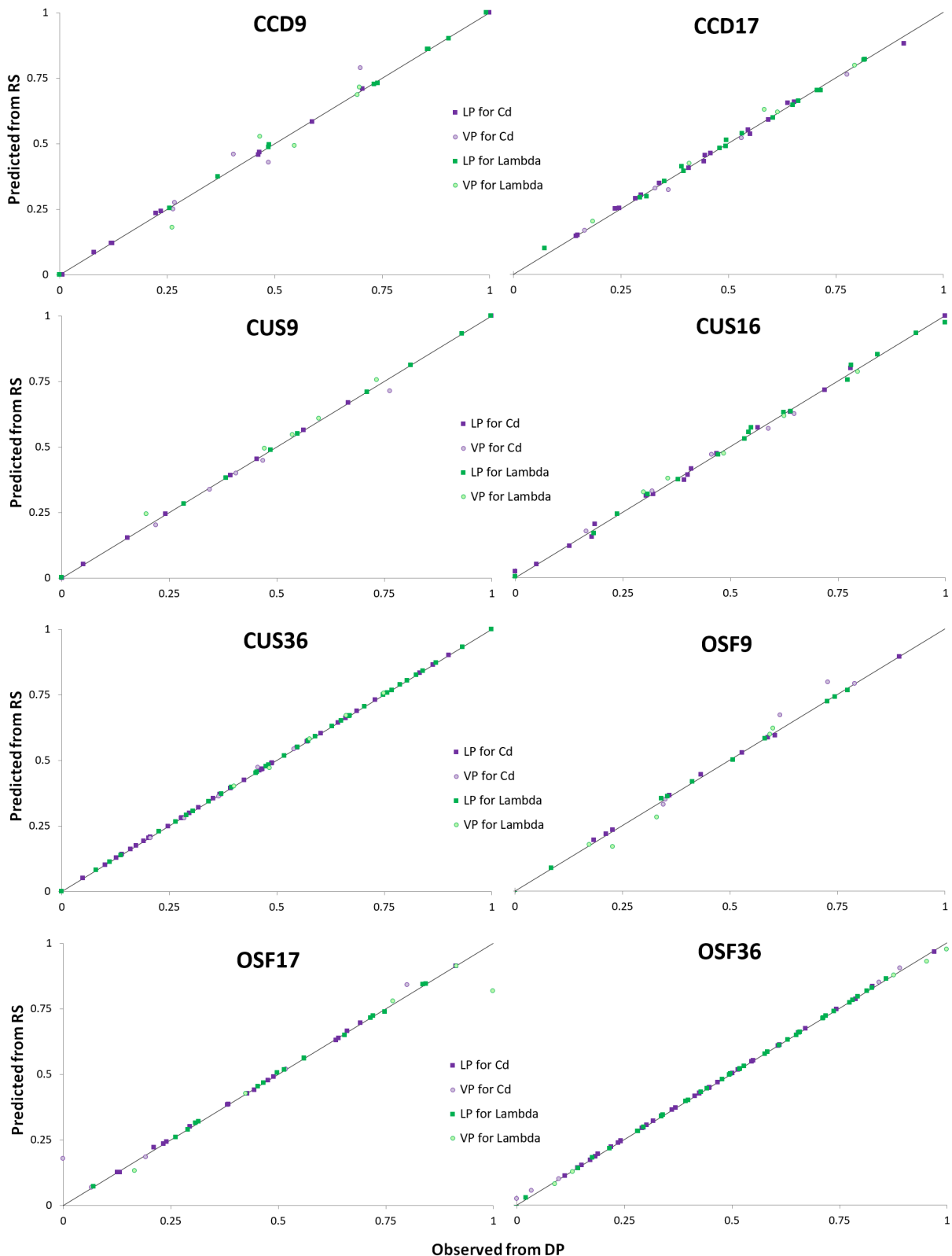


Figure 5.1 – Normalized charts of the predicted-vs-observed values of Cd and aeration for all DOE configurations. Square points are the DOE points and the circular ones are the verification points. The black line represents the line in which the points would have a predicted value from response equal to the observed one in the design points.

Charts in Figure 5.1 show the differences between the quality of fitting for all DOEs. At first glance, it can be seen that the number of simulations influences much more the quality than the spatial distribution of the points. In principle, OSF36 and CUS36 are the DOE candidates for the future analysis, but a deeper study is needed.

To achieve more information about the quality of DOEs, the statistical criteria are shown in Table 5.1 and Table 5.2⁹.

Cd	CCD9	OSF9	CUS9	CCD17	OSF17	CUS16	OSF36	CUS36
Coefficient of Determination (Best value = 1)								
Learning Points	0.9996	0.9991	1.0000	0.9969	0.9987	0.9979	0.9999	1.0000
Verification Points	0.8833	0.9556	0.9785	0.9905	0.9272	0.9904	0.9987	0.9984
Cross-Validation	0.9987	0.9994	0.9994	0.9923	0.9957	0.9917	0.9971	0.9971
Root Mean Square Error (Best value = 0)								
Learning Points	6.403E-07	1.275E-06	6.019E-08	3.620E-06	5.365E-08	4.586E-06	1.199E-07	1.105E-08
Verification Points	6.638E-05	4.639E-05	2.150E-05	1.245E-05	5.019E-05	9.046E-06	6.065E-06	1.103E-06
Cross-Validation	6.280E-08	1.490E-07	5.150E-04	1.230E-03	9.677E-07	1.720E-03	8.810E-05	5.410E-08
Relative Maximum Absolute Error (Best value = 0%)								
Learning Points	3.63	5.48	0.78	15.09	4.32	8.60	3.10	1.32
Verification Points	56.22	36.79	28.36	19.07	24.84	14.77	5.61	6.53
Cross-Validation	5.71	18.37	4.50	16.32	13.89	21.45	14.80	8.63
Relative Average Absolute Error (Best value = 0%)								
Learning Points	1.52	2.62	0.41	4.06	3.08	3.78	0.67	0.08
Verification Points	15.66	8.44	6.48	2.08	8.09	2.83	0.41	0.49
Cross-Validation	2.81	6.31	2.06	6.91	5.43	6.50	3.44	1.99

Table 5.1 – Quality criteria calculated for the discharge coefficient results.

Tables 5.1 and 5.2 show that the DOEs with the greatest number of points, together with the CUS9, are the ones with the best quality criteria.

Among the designs with the largest number of points, there is a small improvement in the cross-validation criteria for the distribution of customs points, so it is easy to prefer CUS36 DOE to be used for the study of physical behavior and optimization. Considering only the learning points, i.e. looking at the quality of the interpolation, we could say that all DOEs except CCD17 produce good results. However, when we look at the verification points, i.e. when the quality of the prediction is considered, the results vary significantly. For example, OSF17 and CCD9 do not predict well enough. CUS9 DOE initially seemed a good candidate to consider even with few points, but when you take into account the quality of the prediction, which is even more important than the quality of the interpolation, the results become unsatisfactory for our study.

⁹To facilitate the visualization of the global qualities of DOEs, the tables have been painted with a conditional format. The greenest box corresponds to the value closest to the best, and the reddest one to the worst.

Lambda	CCD9	OSF9	CUS9	CCD17	OSF17	CUS16	OSF36	CUS36
Coefficient of Determination (Best value = 1)								
Learning Points	0.9996	0.9991	1.0000	0.9972	0.9996	0.9973	0.9999	1.0000
Verification Points	0.8945	0.9608	0.9802	0.9896	0.9460	0.9912	0.9983	0.9973
Cross-Validation	0.9994	0.9941	0.9999	0.9946	0.9949	0.9944	0.9954	0.9962
Root Mean Square Error (Best value = 0)								
Learning Points	3.273E-05	4.240E-05	2.133E-06	1.060E-04	1.874E-05	1.959E-04	3.726E-06	2.807E-08
Verification Points	2.734E-03	1.272E-03	6.580E-04	4.415E-04	1.210E-04	3.037E-04	2.949E-04	7.050E-05
Cross-Validation	1.510E-06	5.130E-06	2.420E-07	3.800E-06	4.070E-06	5.320E-06	3.190E-06	4.060E-06
Relative Maximum Absolute Error (Best value = 0%)								
Learning Points	4.09	5.18	0.83	12.86	4.96	10.40	2.51	0.13
Verification Points	50.81	33.25	25.87	20.58	29.54	13.74	6.40	9.18
Cross-Validation	16.03	12.86	0.44	15.00	13.84	14.27	13.71	5.69
Relative Average Absolute Error (Best value = 0%)								
Learning Points	1.65	2.67	0.40	4.03	1.44	4.07	0.66	0.06
Verification Points	15.20	8.17	6.51	2.10	4.96	2.76	0.46	0.61
Cross-Validation	7.30	6.71	0.28	5.99	6.82	6.39	4.52	4.21

Table 5.2 – Quality criteria calculated for the aeration results.

With respect to the spatial distributions, there are no major differences between them although the worst choice is a random distribution and the best one is the custom distribution (the uniformly distributed one).

Considering the results above, it seems clear that CUS36 DOE is the best option for the future physical analysis and optimization. However, this does not mean that the other designs are bad, but they are worse. For example, for other studies with numerous input parameters, and the number of executions growing exponentially, CUS16 or CCD17 could be good choices since their results are of enough quality and the number of runs is four times less.

Summing up, the DOE CUS36 will be the used for the rest of this study but the choice of the DOE should depend on the characteristics of each specific case. For general output responses, it is possible to choose one DOE with lesser simulations and to achieve good-enough quality criteria.

5.2 Custom DOE - 36 runs

In this section, we first present the sensitivity analysis of the output parameters to see their global behavior regarding the input parameters. Then, the RS of the most-affecting variables is studied, and finally, the optimization is performed to determine the design points which maximize the aeration along with the injector power.

5.2.1 Local Sensitivities

Local Sensitivity charts are used to display the change of the output based on the variation of each input independently. A positive value of the sensitivity means that as the input parameter increases, the output increases as well; and a negative value means the opposite.

Figure 5.2 shows the sensitivities of the main output parameters, namely, the mass flow rate of the gas, the discharge coefficient, the aeration at the outlet, the injector power rate, the total mass flow rate at the outlet and the maximum velocity magnitude of the gas along the domain.

One of the important aspects that can be appreciated in Figure 5.2 is that the behavior of the mass flow rate of gas, the discharge coefficient and the injector power rate is exactly the same, with the same sensitivity values. These three quantities vary proportionally to the angle and inversely proportional to the height. Besides, their global variation is a 16.5% stronger for the angle than for the height. The total mass flow rate at the outlet can be also included in the previous variables group, even although the sensitivities are not exactly the same.

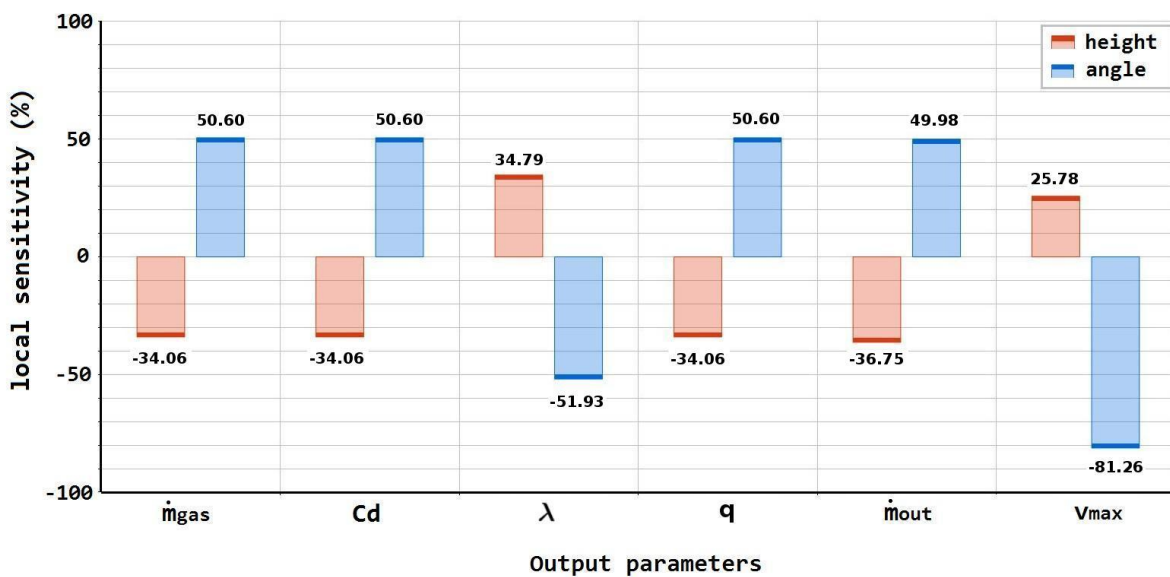


Figure 5.2 – Sensitivities of the output parameters, being \dot{m}_{fuel} the mass flow rate of the entering gas, Cd the discharge coefficient, λ the aeration at the outlet, q the injector power, \dot{m}_{out} the total mass flow rate at the outlet and v_{max} the maximum velocity the gas reaches.

An opposite behavior is found for the aeration and the maximum velocity magnitude. These variables vary proportionally to the height and inversely proportional to the angle. But with different percentages. The maximum velocity is the most-sensitive variable to angle variation, with an 81% negative value, and the lesser sensitive to the height, with almost 26%. Finally,

we can see that the aeration, besides having an opposite behavior to the previously mentioned variables, its sensitivity values are almost the same but with changed sign. This means that, if the height is increased, the aeration will increase by the same quantity as the power rate will decrease, for example.

5.2.2 Response Surfaces

The response surfaces for the discharge coefficient, the aeration, and the maximum velocity of gas will be analyzed since they are the three only variables with different behaviors. Both the standard 3D surface and 2D slides are shown. The 3D surface shows the global variation of output parameters with respect to the inputs. However, without the possibility of rotating the view, the 2D slides are the best option to study the parameters behavior. The 2D slide is a chart that combines the benefits of the 2D and 3D contour graphs by representing a three-dimensional surface in a two-dimensional format.

4.5.2.1 Coefficient of discharge

Figure 5.3 shows 3D responses for the global behavior of Cd regarding the angle for different heights. A curve fitting using Matlab software has been carried out to obtain an analytic expression for the response surface. A five-degree polynomial in two variables is the analytic expression used to fit Cd , the aeration and the maximum velocity. The generic expression for the three outputs is the following one

$$\begin{aligned} f(\tilde{\alpha}, \tilde{h}) = & p_{00} + p_{10} \tilde{\alpha} + p_{01} \tilde{h} + p_{20} \tilde{\alpha}^2 + p_{11} \tilde{\alpha} \tilde{h} + p_{02} \tilde{h}^2 + p_{30} \tilde{\alpha}^3 + p_{21} \tilde{\alpha}^2 \tilde{h} + \\ & p_{12} \tilde{\alpha} \tilde{h}^2 + p_{03} \tilde{h}^3 + p_{40} \tilde{\alpha}^4 + p_{31} \tilde{\alpha}^3 \tilde{h} + p_{22} \tilde{\alpha}^2 \tilde{h}^2 + p_{13} \tilde{\alpha} \tilde{h}^3 + p_{04} \tilde{h}^4 + \\ & p_{50} \tilde{\alpha}^5 + p_{41} \tilde{\alpha}^4 \tilde{h} + p_{32} \tilde{\alpha}^3 \tilde{h}^2 + p_{23} \tilde{\alpha}^2 \tilde{h}^3 + p_{14} \tilde{\alpha} \tilde{h}^4 + p_{05} \tilde{h}^5, \end{aligned}$$

with different coefficients for each output.

The variables have been normalized as follows:

$$\tilde{\alpha} = \frac{\alpha - \bar{\alpha}}{\sigma_\alpha}, \quad \tilde{h} = \frac{h - \bar{h}}{\sigma_h},$$

with means $\bar{\alpha} = 125$ and $\bar{h} = 2.625$, and standard deviations $\sigma_\alpha = 21.05$ and $\sigma_h = 1.428$.

The specific coefficients for Cd are (with 95% confidence bounds):

$$\begin{aligned} p_{00} &= 7.6370 \cdot 10^{-1}, & p_{10} &= 2.9296 \cdot 10^{-2}, & p_{01} &= -2.1881 \cdot 10^{-2}, & p_{20} &= 2.0385 \cdot 10^{-3}, \\ p_{11} &= -9.1310 \cdot 10^{-3}, & p_{02} &= 1.9067 \cdot 10^{-3}, & p_{30} &= 1.9241 \cdot 10^{-3}, & p_{21} &= 1.6708 \cdot 10^{-4}, \end{aligned}$$

$$\begin{aligned}
p_{12} &= 3.4195 \cdot 10^{-3}, & p_{03} &= 4.1194 \cdot 10^{-4}, & p_{40} &= -1.4399 \cdot 10^{-3}, & p_{31} &= 1.8061 \cdot 10^{-4}, \\
p_{22} &= -3.3588 \cdot 10^{-4}, & p_{13} &= -7.2418 \cdot 10^{-4}, & p_{04} &= -1.7457 \cdot 10^{-3}, & p_{50} &= -1.2198 \cdot 10^{-3}, \\
p_{41} &= -1.7969 \cdot 10^{-4}, & p_{32} &= 2.2785 \cdot 10^{-4}, & p_{23} &= 4.6291 \cdot 10^{-4}, \\
p_{14} &= -1.9274 \cdot 10^{-4}, & p_{05} &= 5.8314 \cdot 10^{-4}.
\end{aligned}$$

The Goodness of Fit criteria are $R^2 = 0.9995$ and $RMSE = 8.985 \cdot 10^{-4}$.

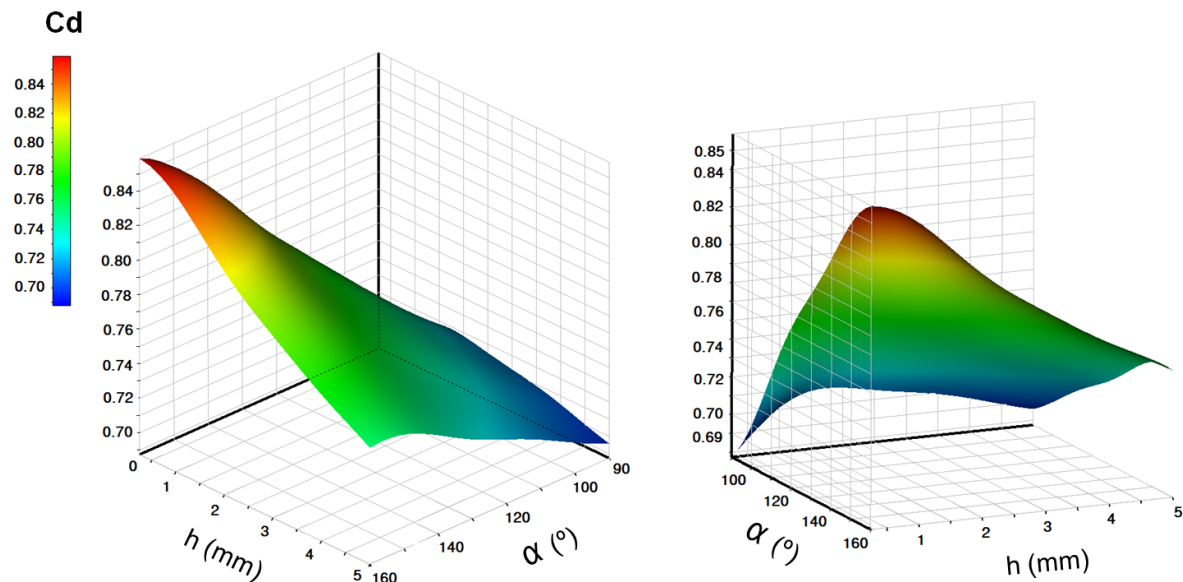


Figure 5.3 – 3D Response surface of the discharge coefficient.

In Figure 5.4, the behavior of Cd with respect to the angle can be analyzed in depth. For the two smaller heights, Cd is a strictly increasing function. For the other heights, Cd reaches the maximum global value about 157° . Therefore, the interesting zone for us (greatest Cd) is $\alpha \in [155, 160]^\circ$.

Besides, it is also observed that the extreme behavior is for the minimum height, $h = 0.25$ mm, where the global minimum and maximum values of Cd are located:

- DP 1 ($h = 0.25$ mm, $\alpha = 90^\circ$) $\longrightarrow Cd_{min} = 0.687$
- DP 6 ($h = 0.25$ mm, $\alpha = 160^\circ$) $\longrightarrow Cd_{max} = 0.859$

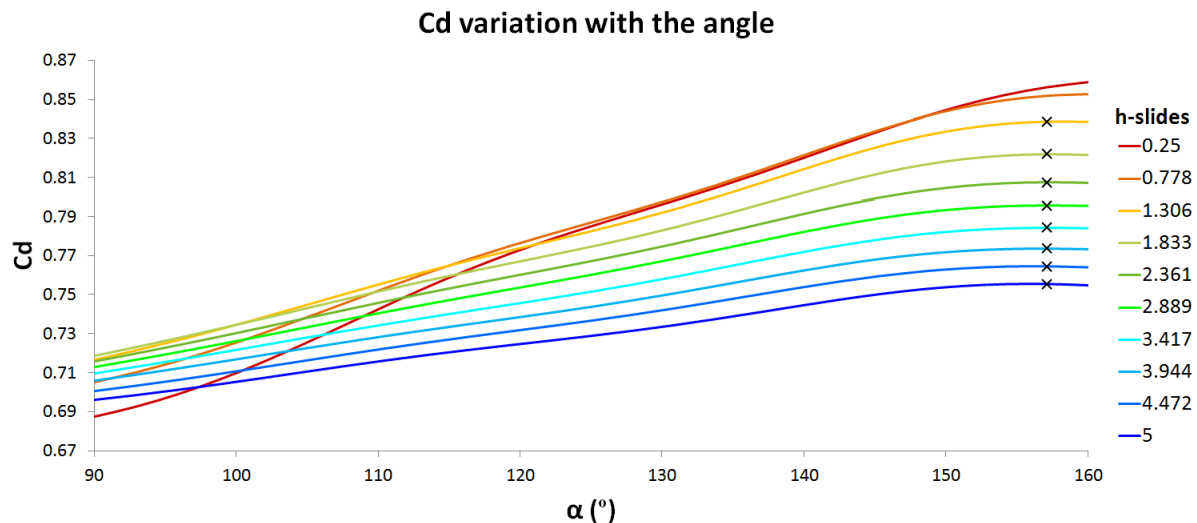


Figure 5.4 – Variation of the discharge coefficient with respect to the angle for different values of height. The cross on the slides represents the location of the maximum point if any.

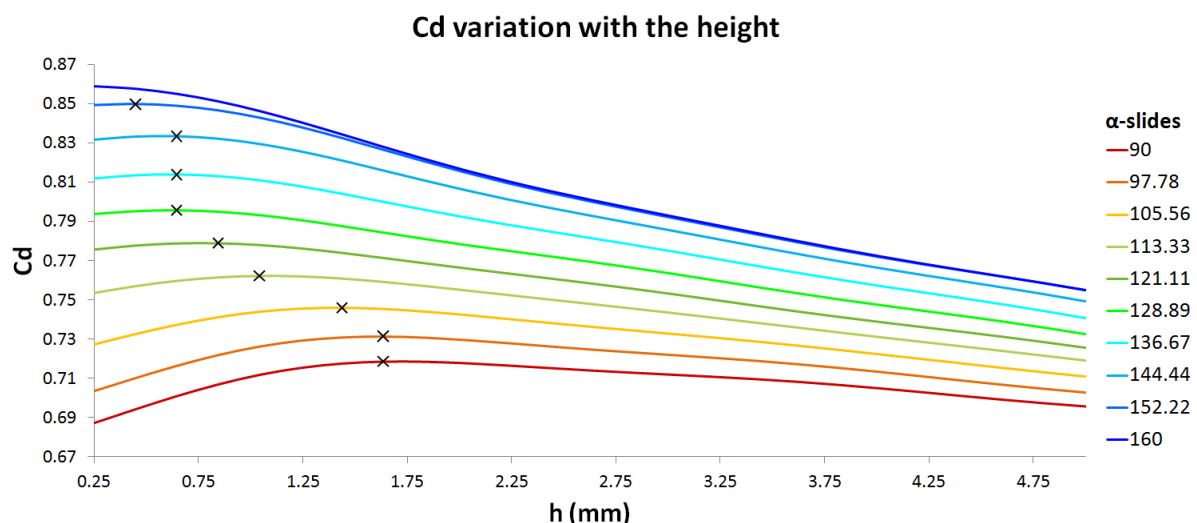


Figure 5.5 – Variation of the discharge coefficient with respect to the height for different values of the angle. The cross on the slides represents the location of the maximum point if exists.

Figure 5.5 represents C_d variation as the height increases for different angles. For all angles, except 160° , the behavior of C_d is increasing until the maximum value and later decreasing. In the graph, it is shown that the maximum points are located at different heights for each angle. As the angle is smaller, the point is farthest from the zero height, varying in a range of $h \in [0.45, 1.64]$ mm. For the 160° -slide, the behavior is strictly decreasing. Figure 5.5 shows that an interesting zone of heights would be between 0.25 mm and 1.75 mm at maximum since

for the rest of the angles and heights, the behavior of Cd is decreasing.

4.5.2.2 Aeration

The aeration at the outlet of the domain respect to the input parameters is represented with a 3D response in Figure 5.6, and with 2D-Slides in Figures 5.7 and 5.8.

For the three dimensional RS, the coefficients of the fitting polynomial are the following

$$\begin{aligned}
 p_{00} &= 7.5635 \cdot 10^1, & p_{10} &= -2.8103, & p_{01} &= 2.0934, & p_{20} &= -5.4872 \cdot 10^{-2}, \\
 p_{11} &= 6.6246 \cdot 10^{-1}, & p_{02} &= -1.2883 \cdot 10^{-1}, & p_{30} &= -1.9574 \cdot 10^{-1}, & p_{21} &= -9.4539 \cdot 10^{-2}, \\
 p_{12} &= -2.5467 \cdot 10^{-1}, & p_{03} &= -3.7045 \cdot 10^{-2}, & p_{40} &= 1.1689 \cdot 10^{-1}, & p_{31} &= 5.0703 \cdot 10^{-3}, \\
 p_{22} &= 7.4373 \cdot 10^{-2}, & p_{13} &= 9.9980 \cdot 10^{-2}, & p_{04} &= 1.6123 \cdot 10^{-1}, & p_{50} &= 1.1394 \cdot 10^{-1}, \\
 p_{41} &= 3.3722 \cdot 10^{-2}, & p_{32} &= -2.8091 \cdot 10^{-2}, & p_{23} &= -6.3424 \cdot 10^{-2}, \\
 p_{14} &= -7.2341 \cdot 10^{-3}, & p_{05} &= -5.0940 \cdot 10^{-2}.
 \end{aligned}$$

The Goodness of Fit criteria are $R^2 = 0.9995$ and $RMSE = 8.475 \cdot 10^{-2}$.

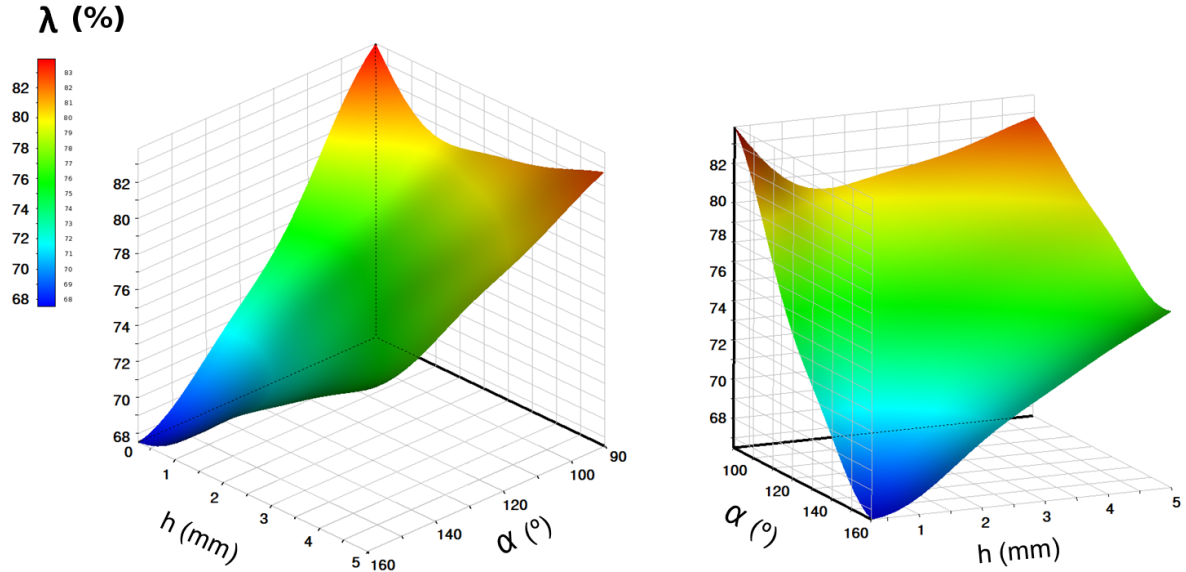


Figure 5.6 – 3D Response surface of the aeration.

As deduced from the sensitivities chart, the behavior of aeration λ is opposite to that of Cd . Regarding the angle, the aeration decreases as the angle increases, reaching the overall minimum for the larger angles; and regarding the height, the aeration decreases until it reaches the

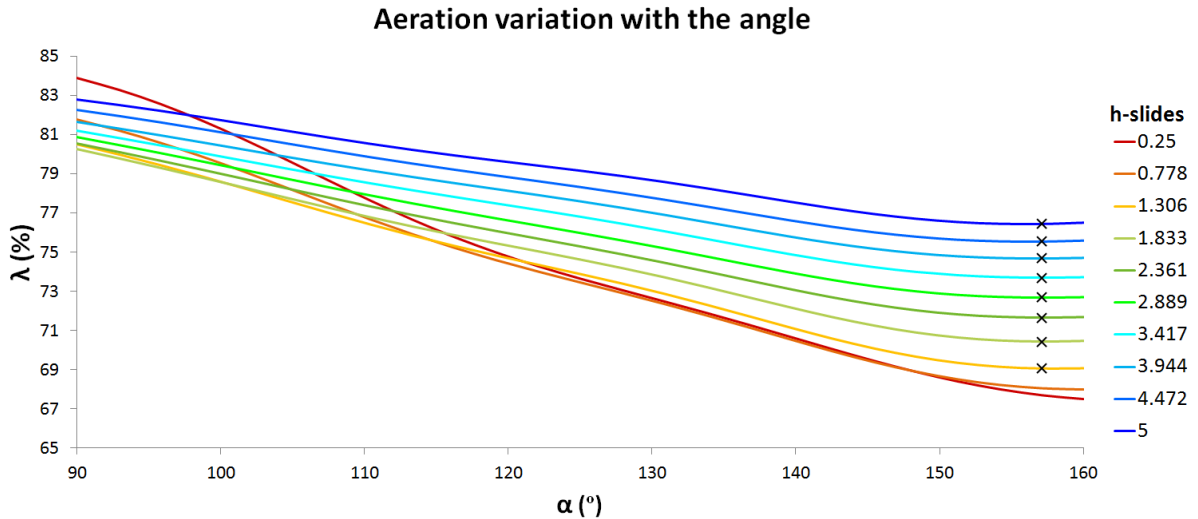


Figure 5.7 – Variation of the aeration with respect to the angle for different values of the height. The cross on the slides represents the location of the minimum point if any.

minimum points (see Figures 5.7 and 5.8). The placement of minimum points is the same as before for Cd . Finally, it is seen that the 160° -slide also has a different behavior than the rest, remaining growing from the beginning.

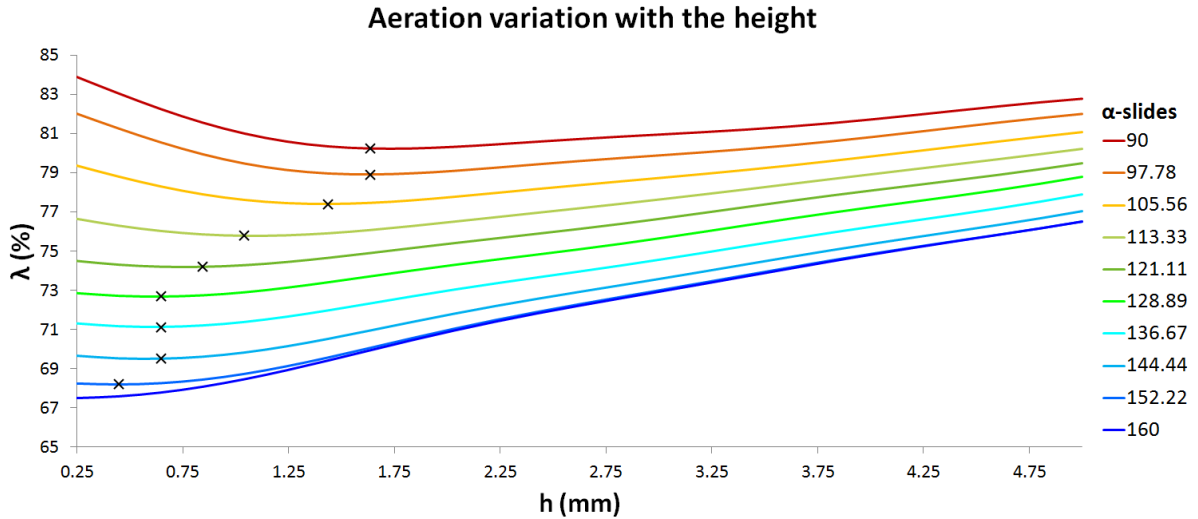


Figure 5.8 – Variation of the aeration with respect to the height for different values of the angle. The cross on the slides represents the location of the minimum point if any.

The global maximum and minimum values correspond to the same design points than before, but interchanged:

- DP 6 ($h = 0.25\text{mm}$, $\alpha = 160^\circ$) $\longrightarrow \lambda_{min} = 67.50\%$
- DP 1 ($h = 0.25\text{mm}$, $\alpha = 90^\circ$) $\longrightarrow \lambda_{max} = 83.88\%$

4.5.2.3 Maximum velocity of gas

The maximum velocity that the mixture reaches is represented with a 3D response in Figure 5.9, and with 2D-Slides in Figures 5.10 and 5.11.

For the three dimensional RS, the coefficients of the fitting polynomial are the following:

$$\begin{aligned}
 p_{00} &= 7.8300 \cdot 10^1, & p_{10} &= 9.6604 \cdot 10^{-2}, & p_{01} &= -2.3080 \cdot 10^{-1}, & p_{20} &= 2.0352 \cdot 10^{-1}, \\
 p_{11} &= 1.5971 \cdot 10^{-1}, & p_{02} &= 1.2336 \cdot 10^{-1}, & p_{30} &= -3.4766 \cdot 10^{-1}, & p_{21} &= -1.2979 \cdot 10^{-1}, \\
 p_{12} &= 2.1573 \cdot 10^{-2}, & p_{03} &= 1.4581 \cdot 10^{-1}, & p_{40} &= 4.3150 \cdot 10^{-2}, & p_{31} &= -1.9186 \cdot 10^{-2}, \\
 p_{22} &= -1.2147 \cdot 10^{-1}, & p_{13} &= -4.8089 \cdot 10^{-2}, & p_{04} &= -7.8389 \cdot 10^{-2}, & p_{50} &= 3.0064 \cdot 10^{-2}, \\
 p_{41} &= 3.0702 \cdot 10^{-2}, & p_{32} &= 1.0746 \cdot 10^{-1}, & p_{23} &= 2.1816 \cdot 10^{-2}, \\
 p_{14} &= -2.3669 \cdot 10^{-2}, & p_{05} &= -3.9661 \cdot 10^{-3}.
 \end{aligned}$$

The Goodness of Fit criteria are $R^2 = 0.9868$ and $RMSE = 5.074 \cdot 10^{-2}$.

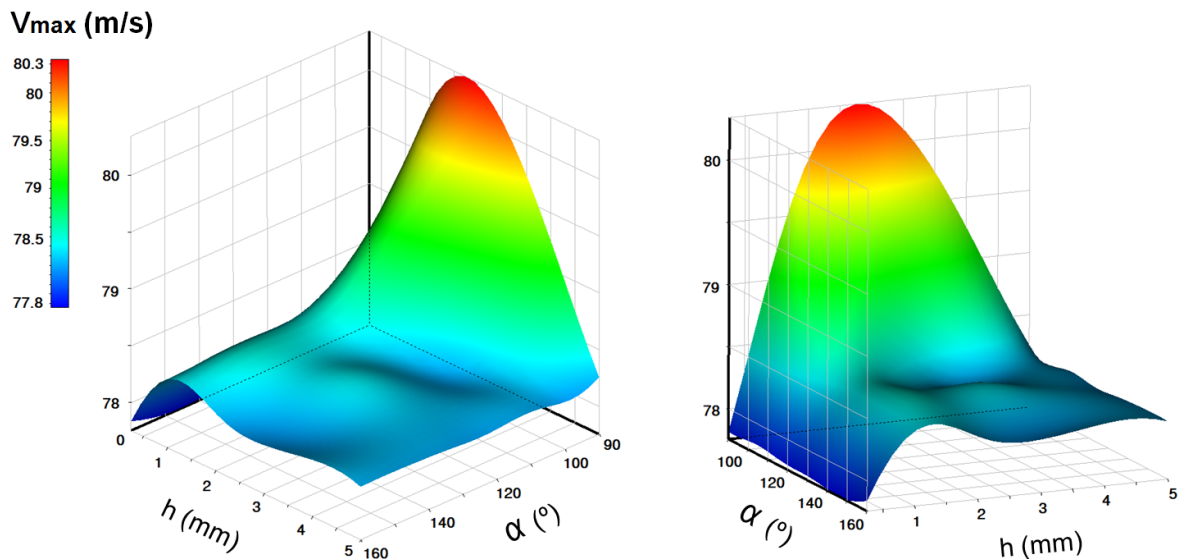


Figure 5.9 – 3D Response surface of the maximum velocity of gas.

From Figures 5.10 and 5.11, it can be concluded that the variation with the angle is such that for angles greater than 120° , the velocity is approximately constant at all heights, oscillating around 78.3 and 78.6 m/s; except for the 0.25-height, in which the effect of the angles is negligible, and the velocity remains constant (77.8 m/s). Starting at 90° , the behavior of maximum velocity is decreasing until 120° approximately, where it stabilizes.

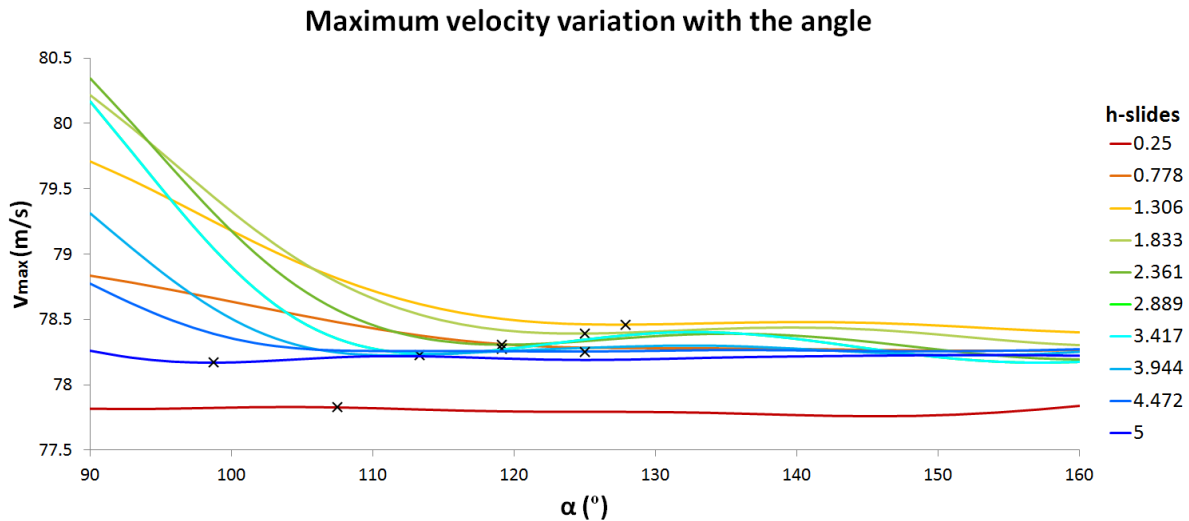


Figure 5.10 – Variation of the maximum velocity of gas with respect to the angle for different values of the height. The cross on the slides represents the location of the first inflection point.

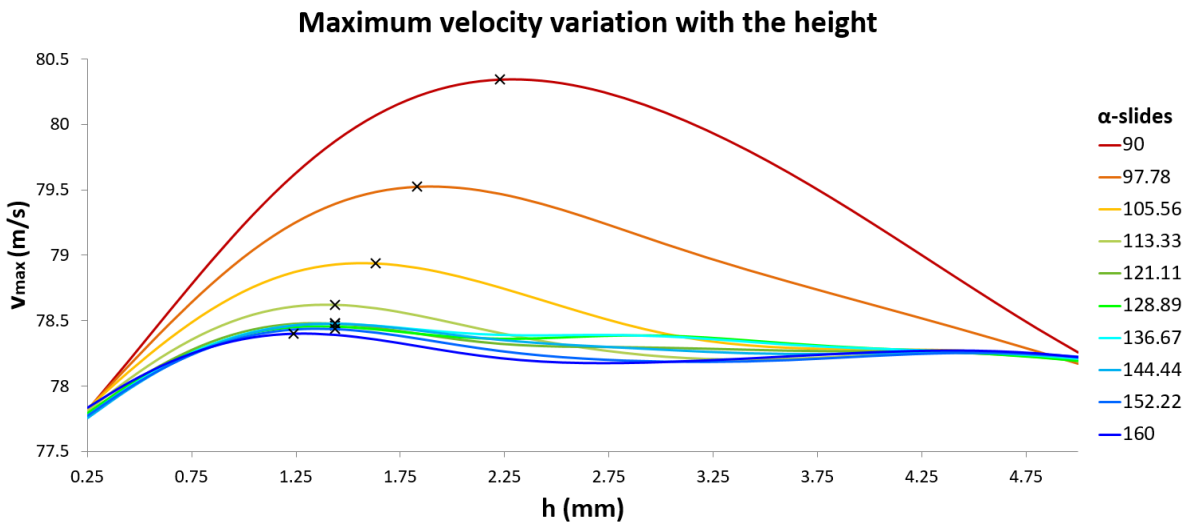


Figure 5.11 – Variation of the maximum velocity of gas with respect to the height for different values of the angle. The cross on the slides represents the location of the maximum point if any.

Regarding the variation with respect to the height (Figure 5.11), all velocities grow until they reach the global maximum value. Maximum velocity variation is achieved for the smallest angles. In addition, as the angle increases, the curve flattens slowly.

Summing up, the response of the maximum velocity may be considered as constant for $\alpha > 120^\circ$ and $h > 1$ mm; as increasing for heights between 0.25 and 1 mm; and as decreasing for angles between 90 and 120° .

5.2.3 Optimization

The MOGA method has been used to perform the Response Surface Optimization. The aim is to obtain injector configurations that meet physical constraints sought in the gas burner design. For example, one of them is the improvement of air entrainment, i.e. maximizing the aeration. Another one could be to maximize the discharge coefficient to minimize power losses. In the first place, our target has been to maximize the aeration at the same time as the discharge coefficient since they are variables with opposite behaviors, and it is desired to increase the aeration, but without losing injector power rate.

MOGA method uses a genetic algorithm to generate the initial samples and then iterates to find feasible points. Here, it has used 173 iterations to achieve a Pareto percentage of 88%. The Pareto percentage used by ANSYS is a percentage that represents the ratio of the number of desired Pareto points to the number of samples per iteration. The default convergence criteria in ANSYS is a Pareto percentage of 70%.

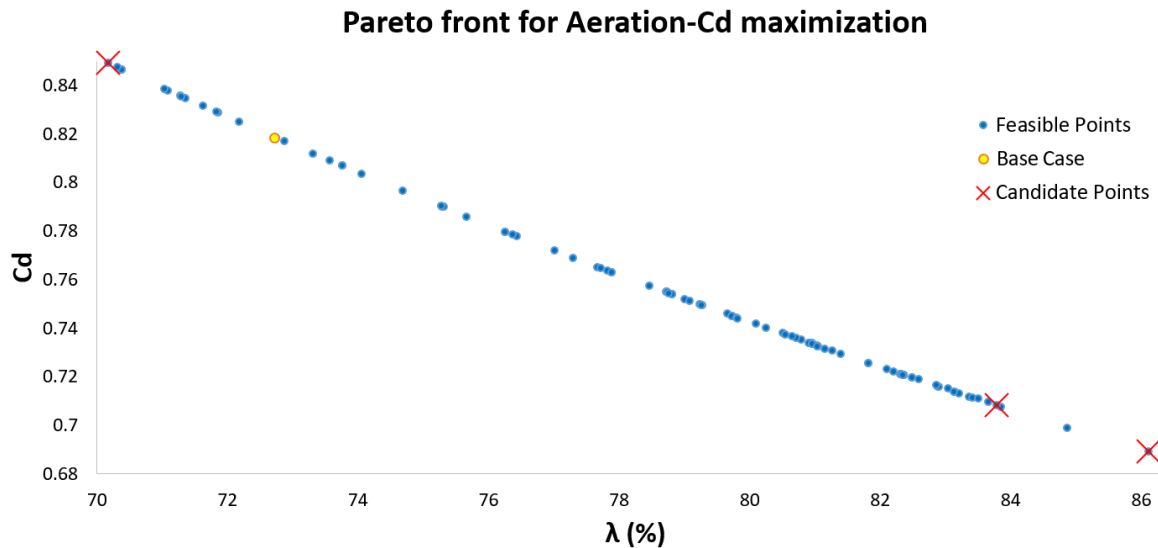


Figure 5.12 – Pareto front obtained by maximizing aeration and discharge coefficient.

The corresponding value for the base case is plotted in yellow.

The Pareto front obtained in the first multi-objective optimization is represented in Figure 5.12. The objective this time was maximizing aeration and Cd . As expected, it can be seen that there are no optimal points that achieve maximization in both variables. In fact, for all feasible points, if the aeration is increased, the discharge coefficient always decreases. Then, the optimal solutions for this case will depend on other additional restrictions and preferences for each case. ANSYS proposes three candidate points, which are the following:

	h (mm)	α (°)	λ (%)		Cd	
			Parameter value	Variation from reference	Parameter value	Variation from reference
Candidate Point 1	0.27	90.3	★★ 86.1	2.8%	✗ 0.689	-2.7%
Candidate Point 2	0.61	152.9	✗✗ 70.2	16.3%	★★ 0.850	19.9%
Candidate Point 3	4.45	97.5	★★ 83.8	0.0%	✗✗ 0.708	0.0%

Table 5.3 – Candidate points proposed by ANSYS software in λ - Cd maximization.

The three candidate points correspond to extreme parameter values. As we saw in the results section, for small angles and small heights the aeration increases; and for large angles and small heights, it is the discharge coefficient that increases. The table shows that for the first candidate point, the discharge coefficient decreases in the same percentage as the aeration increases, but for the second point, although aeration is lost with respect to the reference, the increase in the discharge coefficient is greater than the loss by 3.6%.

In a second multi-objective optimization process, an additional constraint was added to see the influence on the results and whether the number of feasible points was reduced. Besides the above restrictions, the requirement that the power rate be equal to or greater than the base case power rate was included. Now ANSYS has needed 245 iterations and has achieved the minimum Pareto percentage required, 70%. The Pareto front is shown in Figure 5.13.

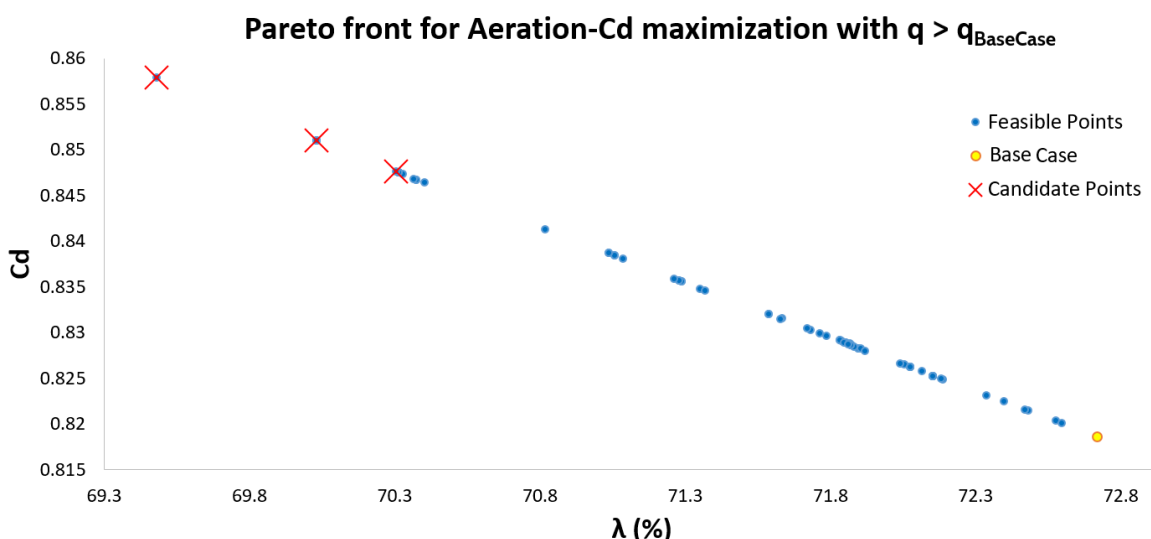


Figure 5.13 – Pareto front obtained by maximizing of aeration, discharge coefficient and the power. The power rate has to be equal to or greater than the base case power.

Since the discharge coefficient and the injector power rate have proportional behaviors, the new

feasible points are all above the base case. The candidate points now are the three ones with the highest Cd (Table 5.4).

	h (mm)	α (°)	λ (%)		Cd		q (W)	
			Parameter value	Variation from reference	Parameter value	Variation from reference	Parameter value	Variation from reference
Candidate Point 1	0.42	159.4	XX 69.5	-1.2%	★★ 0.858	1.2%	★★ 1953.3	1.2%
Candidate Point 2	0.61	154.2	XX 70.0	-0.4%	★★ 0.851	0.4%	★★ 1937.5	0.4%
Candidate Point 3	0.60	151.2	XX 70.3	0.0%	★★ 0.848	0.0%	★★ 1929.9	0.0%

Table 5.4 – Candidate points proposed by ANSYS software in $\lambda - Cd - q > q_{basecase}$ maximization.

All these points correspond to very small heights and very large angles, which implies high discharge coefficients and therefore bad aeration. It can be seen that the new restriction only provides a reduction in the range of achievable points, delimiting it to those points above the base case. However, as far as the quality of the results is concerned, they are similar to the previous ones. Again, the gains in Cd are equivalent to the losses in aeration, although, with this new condition, we can eliminate points with great heights.

So far we have seen that the optimization of these two variables does not provide as satisfactory results as would have been desired. However, we can conclude that in order not to have losses in power rate we must work with small heights ($\approx 0.5\text{mm}$) and extreme angles ($\approx 155^\circ$).

Therefore, in view of the above results, it was introduced the maximum gas velocity in the multi-objective optimization process, as it is a variable independent of aeration and discharge coefficient and perhaps the results may produce different conclusions. This time ANSYS has needed 669 iterations with the minimum Pareto percentage required, 70%.

A high gas velocity should mean better aeration as the jet can drag more air due to a higher momentum. This new Pareto front (Figure 5.14) shows an inverse behavior for aeration and gas velocity. In fact, higher gas velocities drag more air, but the injectors that produce higher velocities are the ones with higher powers. This translates into a greater mass flow rate at the gas inlet, and therefore a decrease in lambda.

However, the new candidate points (see Table 5.5) differ from those got previously. Now the proposal is the minimum angle together with heights of approximately 2.5mm. These configurations may seem good findings but comparing the discharge coefficient values with the value of the base case, we see that they are much lower and therefore the power rate is also lower. That

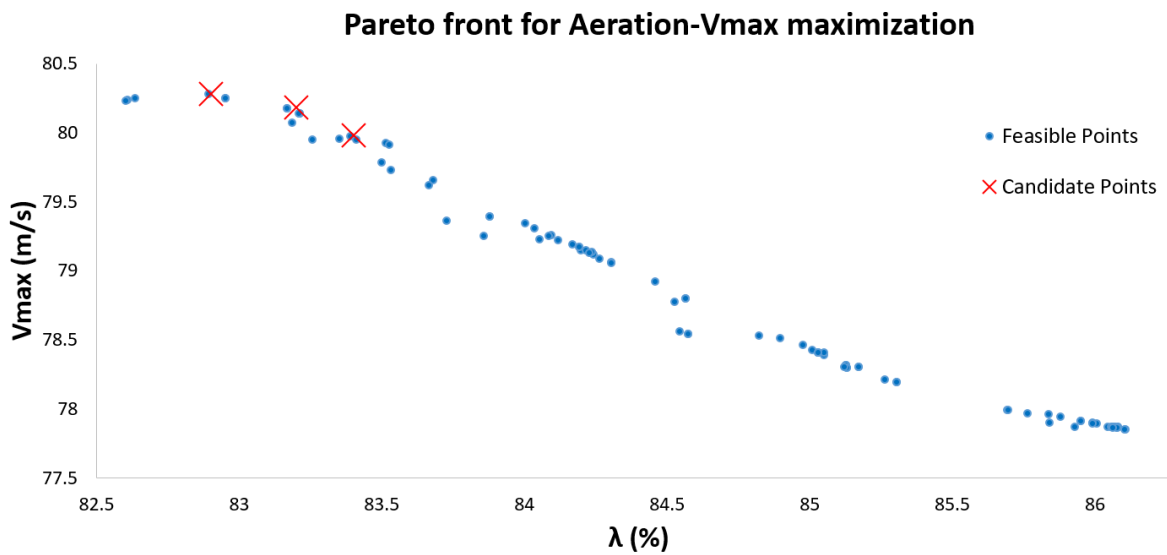


Figure 5.14 – Pareto front obtained by maximizing aeration and gas velocity.

is to say, the maximum velocity and the aeration get a good multi-objective optimization by themselves, but when the power rate is considered we arrive to the same situation as before.

	h (mm)	α ($^{\circ}$)	λ (%)		V_{max} (m/s)		Cd
			Parameter value	Variation from reference	Parameter value	Variation from reference	
Candidate Point 1	2.39	90.4	★★ 82.9	-0.6%	★★ 80.28	0.4%	0.716
Candidate Point 2	2.78	90.4	★★ 83.2	-0.3%	★★ 80.18	0.3%	0.713
Candidate Point 3	3.15	90.4	★★ 83.4	0.0%	★★ 79.98	0.0%	0.711

Table 5.5 – Candidate points proposed by ANSYS software in λ - Cd - V_{max} maximization.

Our goal of increasing aeration and not losing power rate is only achievable by compromising one of the two variables. However, it has been seen that small heights with larger angles give better results for that purpose. When we introduce maximum gas velocity maximization, the results improve, as the overall maximum values are also reached for high lambda values. The disadvantage is that these cases have lost power. To conclude, it can be said that we have obtained a Pareto front with achievable point ranges and global guidelines for maximizing aeration. Depending on each specific case, or on the variables to be analyzed, different objectives must be added and a compromise must be reached in the optimization.

Chapter 6

Concluding remarks

*We can only see a short distance ahead, but we can see
plenty there that needs to be done.*

Alan Turing

6.1 Conclusions

Design Exploration tools

The Design Exploration process has been carried out to efficiently analyze the influence of the internal geometry of gas burner injectors on its performance. Besides, the different mathematical tools used in the process have been studied.

Regarding the DOEs, it has been seen that the number of simulations has much more influence in the quality of results than the spatial distribution of design points. In fact, except for DOEs with 36 simulations, the global quality got in the rest is not enough to consider them as acceptable for this project. When considering those DOEs with 36 design points, the custom spatial distribution provides slightly better results, although as a general line the optimal space filling (random) is also a good choice.

The Genetic Aggregation algorithm has been used to create the response surfaces. Despite being slower, it has been proven to be the most recommendable option to use, since it tests the rest of the algorithms and chooses the best according to the characteristics of each case.

Nevertheless, it is crucial to study in depth the quality metrics to determine if the response is fine enough or if refinement points are required.

Physical behavior

Considering the physical variables behavior with respect to the studied geometric injector parameters, the following fundamental conclusions are in order: (Figure 6.1 is placed here for the convenience of the reader, but is the same that Figure 5.2):

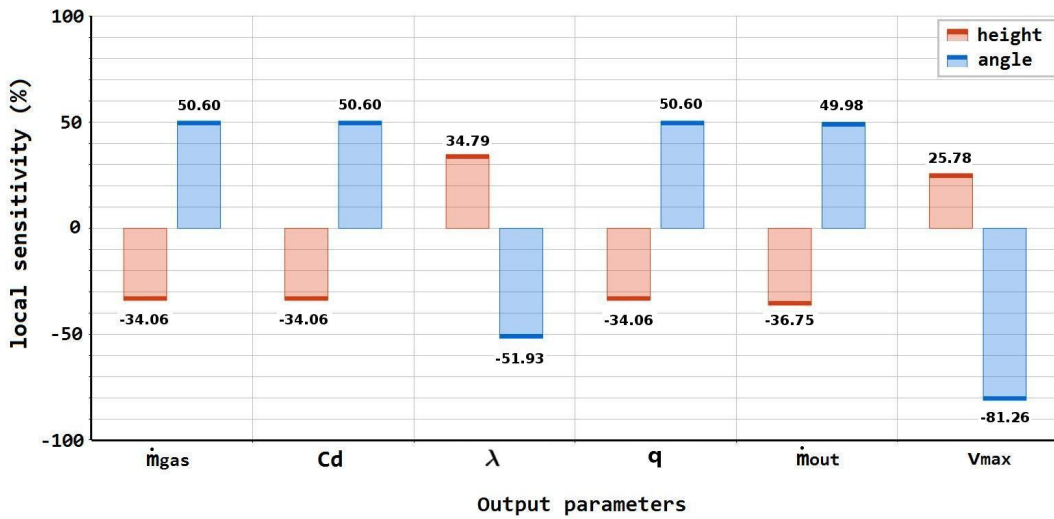


Figure 6.1 – Sensitivities of the output parameters.

1. The mass flow rate of the gas in the injector inlet (\dot{m}_{gas}), the discharge coefficient (C_d) and the injector power rate (q) have the same behavior respect to the angle and the height. They increase as the angle increases with a sensitivity of 50.6%; and they decrease with the height with a sensitivity of -34.06%. Therefore, the global variation of these outs is a 16.5% stronger for the angle than for the height.
2. The mass flow rate of the mixture at the outlet (\dot{m}_{out}) has sensitivities extremely near to the previous ones, with a 49.98% for the angle, and -36.75% for the height. Therefore, if the mass flow rate of the fuel at the injector inlet and the mass flow rate of the mixture at the outlet have the same behavior and sensitivities, the conclusion is that the effect of the air entrainment is negligible.
3. The behavior of the aeration and the maximum velocity of the gas is opposite than before. If the height increases they also increase, and they decrease when the angle increases. The velocity of gas is the most sensitive variable, having a sensitivity of 25.78% for the height, and -81.26% for the angle. Regarding the aeration, the sensitivities are 34.79% for the

height, and -51.93% for the angle; that is, totally opposed to q , Cd , etc.

$$\dot{m}_{gas}, Cd, q, \dot{m}_{out} \leftarrow \text{opposite behaviors} \rightarrow \lambda, v_{max}$$

Regarding the multi-objective optimization, it has been seen that our goal of increasing aeration and not losing power rate is only achievable by compromising one of the two variables. In future cases, other additional requirements must be added for achieving optimal points, optimize other variables or even better, other geometrical parameters.

Geometric analysis

In the optimization part, it has been seen that small heights with larger angles give better results for maximizing aeration and injector power rate. On the other hand, the relevant geometrical conclusions for general gas burner injectors design are:

1. The discharge coefficient increases as the angle increases to approximately 157° . Thus, a relevant interval in which we should focus on for designing is $\alpha \in [155, 160]^\circ$.
2. Considering the height, from 1.75mm the discharge coefficient is decreasing and the interesting zone for design is $h \in [0.25, 1.75]$ times the injector diameter.

6.2 Future work

This project can be extended in future to analyze another main group of injectors, the so-called *counter-bored injectors*. As shows Figure 6.2 they have very different internal shape than the ones analyzed in this project. The study carried out of DOEs will be very helpful here because the choice of one of them is critical since the number of geometrical parameters for these injectors is bigger and a compromise between the number of them and the number of design points will need to be reached.

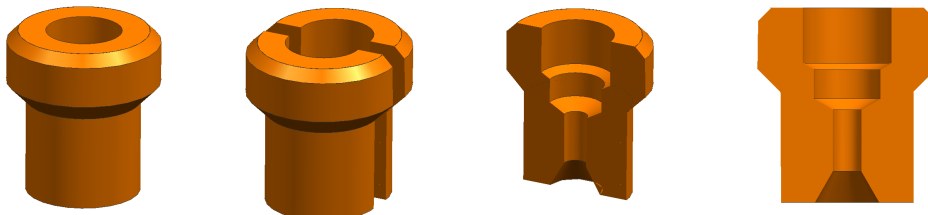


Figure 6.2 – Geometry example of counter-bored injectors.

Also, the analysis can be completed including other burner elements such as the Venturi tube or the spreader for example.

Appendices

Appendix A

Fluid concepts

A.1 Fluid numbers

Reynolds number (Re)

It is an important parameter that appears in numerous problems of fluid mechanics because it allows working with the dimensionless Navier-Stokes equations. This number relates the kinematic viscosity of a fluid (ν) characteristic velocity and length of a problem (v_0 and l_0), and it represents how greater are the viscous forces with respect to the inertial ones. It is given by

$$Re = \frac{v_0 l_0}{\nu}. \quad (\text{A.1})$$

High Reynolds numbers indicate that inertial forces predominate versus viscous, and for high enough numbers, the flow will be turbulent. For low Reynolds numbers, the flow will be laminar.

Wobbe index (W)

It measures the interchangeability of two gases when they are used as a fuel [1]. It is essential for analyzing the impact of a fuel changeover and is also a common specification of appliances that use gas and of devices that transport gas. Two gases with the same Wobbe index should supply the same heat flow into a combustion process per unit of volume.

Wobbe index can be calculated as follows,

$$W = h_s \left(\frac{\rho_{fuel}}{\rho_a} \right)^{1/2} \quad \text{kJ/m}^3, \quad (\text{A.2})$$

where ρ_{fuel} and ρ_a are the densities of fuel and air respectively and h_s is the calorific value of the gas.

Prandtl number (Pr)

It is defined as the ratio between momentum and the thermal diffusivity. Thus,

$$Pr = \frac{\mu/\rho}{k/(C_p \rho)} = \frac{C_p \mu}{k}, \quad (\text{A.3})$$

where C_p is the specific heat at a constant pressure. Prandtl number depends only on the fluid.

Turbulent Prandtl number

The concept of a turbulent Prandtl number is useful for solving the heat transfer problem of turbulent boundary layer flows. It is defined as the momentum eddy viscosity divided by the heat transfer eddy viscosity:

$$\sigma_{k,\varepsilon} = \frac{\epsilon_M}{\epsilon_H}. \quad (\text{A.4})$$

More information about P_{rt} and its derivation from the energy and momentum equations can be found in [21].

Eckert number (Ec)

E_c [28] is a non-dimensional quantity that compares the kinetic energy of the flow with the enthalpy. It is given by

$$E_c = \frac{v^2}{C_p T}. \quad (\text{A.5})$$

In a heat transfer situation the Eckert number is useful in determining the relative importance of the kinetic energy of a flow.

A.2 Diffusive fluxes

Diffusive flux of species

The diffusive flux of a species α (\mathbf{J}_α) has three components: the gradient of species, the gradient of temperature (Soret effect) and the gradient of pressure [29]. The effect of pressure and temperature gradients are usually neglected in combustion fluxes [28]. Therefore, the diffusive flux, \mathbf{J}_α , only considers the mass diffusion due to the gradient of species, according to Fick's Law [19, 29]. The diffusive flux of species can be written as follows:

$$\mathbf{J}_\alpha = -\Gamma_\alpha \nabla Y_\alpha, \quad \Gamma_\alpha = \frac{\mu}{S_{c_\alpha}}, \quad (\text{A.6})$$

in terms of the Schmidt number of species, S_{c_α} , defined as:

$$S_{c_\alpha} = \frac{\mu}{D_\alpha \rho}. \quad (\text{A.7})$$

The term D_α represents the diffusion coefficient of a species α [29].

Heat diffusive flux

The heat diffusive flux, \mathbf{J}_h , has also three components in general. Namely, the gradient of temperature (Fourier's Law), the gradient of concentrations (Dufour effect) and the last one related to the diffusive flux of species. In combustion fluxes, the last two terms are often neglected [28, 29]. Thus, the term \mathbf{J}_h is expressed by the Fourier's Law as follows:

$$\mathbf{J}_h = -\kappa \nabla T, \quad (\text{A.8})$$

κ being the thermal conductivity of the mixture and T the temperature.

Nomenclature

Greek Symbols

α	Injector angle parameter
α_b	Injector angle for the base case
$\epsilon(p_i)$	Estimation error in response surface
κ	Thermal conductivity
λ	Aeration
μ	Dynamic viscosity
μ_t	Turbulent viscosity
ν	Kinematic viscosity
ϕ	Viscous dissipation term
ρ	Mixture density
ρ_a	Air density
ρ_{fuel}	Fuel density
σ	Relative gas density
σ_r	Standard deviation of r_j values
$\sigma_{k,\varepsilon}$	Turbulent Prandtl numbers
ε	Dissipation rate
φ	Generic field variable in Favre averaging
φ'	Perturbation of a generic variable φ

$\tilde{\varphi}$ Mean part of the generic variable φ

τ Stress tensor

Roman Symbols

A_i Injector area

$C_{1,2,3\varepsilon}$ Closure coefficients of turbulence model

C_μ $k - \varepsilon$ model constant

$C_{p,\alpha}$ Specific heat at constant pressure of species α

Cd Discharge coefficient

Cv Gas calorific value

D Injector diameter

D_b Injector diameter of the base case

D_α Diffusion coefficient of a species α

E Total energy

Ec Eckert number

f Body forces vector

g Gravity acceleration

G_b Turbulence kinetic energy generation due to buoyancy

G_k Turbulence kinetic energy generation due to mean velocity gradients

h Injector height parameter

h_b Injector height for the base case

h_s Heat of combustion

h_g Height of a column of gas required to exert the gas pressure in the injector

H Enthalpy

H_α Specific enthalpy for species α

H_α^0	Specific enthalpy of formation
\mathbf{I}	Identity tensor
\mathbf{J}_α	Diffusive flux of α species
\mathbf{J}_H	Heat diffusive flux
k	Turbulence kinetic energy
K	Kinetic energy
l_0	Characteristic length
L_i	Number of levels of a parameter
m_T	Total mass of the mixture
m_α	Mass of the α species
m_{air}	Mass of the air
m_{gas}	Mass of the fuel
\dot{m}_{gas}	Mass flow rate of the fuel
M_α	Molecular weight of α species
\overline{M}	Average molecular weight
N	Number of sampling points
N_p	Number of parameters
N_α	Number of chemical species
P	Number of polynomial terms in quadratic RS, except the constant term
p	Total pressure
p_i	Parameters
p_{atm}	Atmospheric pressure
p_g	Gauge pressure
Pr	Prandtl number

q	Heat flow
r	Generic response variable
\bar{r}	Arithmetic mean of the values of r_j
\tilde{r}	Response surface regression model
r_j	Value of the output parameter in the j-th sampling point
\tilde{r}_j	Value of the regression model at the j-th sampling point
R	Universal gas constant
R^2	Coefficient of determination
Re	Reynolds number
S_α	Net formation of the α species
S_c	Schmidt number
S_H	Volumetric source for H
$S_{k,\varepsilon}$	User-defined sources for k and ε
t	Time
T	Temperature
T_0	Reference temperature
u	Internal energy
U	Potential energy
v_0	Characteristic velocity
\mathbf{v}	Fluid velocity
\dot{V}	Volume flow rate
W	Wobbe index
$x_{i,j}$	Cartesian coordinates
Y_α	Mass fraction of an α species

Y_M Fluctuating dilatation

Abbreviations and acronyms

AFR Air-Fuel Ratio

AMO Adaptive Multi-Objective

ASO Adaptive Single-Objective

BBD Box-Behnken Design

CAD Computer-Aided Design

CAE Computer-Aided Engineering

CCD Central Composite Design

CFD Computational Fluid Dynamics

DO Direct Optimization

DOE Design Of Experiments

DP Design Point

GOF Goodness of Fit

LHS Latin Hypercube Sampling

MISQP Mixed-Integer Sequential Quadratic Programming

MOGA Multi-Objective Genetic Algorithm

NLPQL Nonlinear Programming by Quadratic Lagrangian

OSF Optimal Space Filing

PDE Partial Differential Equations

RMSE Root Mean Square Error

RS Response Surface

RSO Response Surface Optimization

SGI Sparse Grid Initialization

Bibliography

- [1] Annamalai, K. and Puri, I. K. (2007). Combustion science and engineering. *CRC Press*.
- [2] ANSYS Inc. (2018) <https://www.ansys.com/es-es>
- [3] ANSYS Inc. (2017). ANSYS DesignXplorer User's Guide.
- [4] ANSYS Inc. (2016). ANSYS DesignXplorer Workshop. Lectures trainee.
- [5] ANSYS Inc. (2017). ANSYS Fluent Theory's Guide.
- [6] ANSYS Inc. (2017). ANSYS Fluent User's Guide.
- [7] Aris, R. (1962). Vectors, Tensors and the Basic Equations of Fluid Mechanics. *Dover Publications*.
- [8] Batchelor, G. K. (2000). An Introduction to Fluid Dynamics. *Cambridge Mathematical Library*. *Cambridge University Press*.
- [9] Bosch Group (2018) <https://www.bsh-group.com>
- [10] Box, G. E. P., and Wilson, K. B. (1951). On the experimental attainment of optimum conditions. *Journal of the Royal Statistical Society. Series B* Vol. 13, N° 1, pp. 1-45.
- [11] Cavazzuti, M. (2013). Optimization Methods: From Theory to Design *Springer*.
- [12] Chen, C., Riley, J. J. and McMurty, P. A. (1991). A Study of Favre Averaging in Turbulent Flows with Chemical Reaction.
- [13] Chorin, A. J. and Marsden, J. E. (1990). A Mathematical Introduction to Fluid Mechanics. Department of Mathematics, University of California.
- [14] Courant, R., Friedrichs, K. and Lewy, H. (1967). On the Partial Difference Equations of Mathematical Physics. *IBM Journal of Research and Development*, volume 11 (2), pp. 215 - 234.

- [15] Cox, D. R. and Reid, N. (2000). The Theory of the Design of Experiments. *Chapman and Hall / CRC*.
- [16] Crespo, A. (2002). Mecánica de fluidos. Universidad Politécnica de Madrid. *Escuela Técnica Superior de Ingenieros Industriales. Servicio de Publicaciones*.
- [17] European Standard, "DIN EN 30-2-1:1998 Part 2-1: Rational use of energy – General," in Domestic cooking appliances burning gas, p. 10
- [18] Fueyo, N. (2010). Fundamentos de Fluidos y Procesos Fluidomecánicos. *Área de Mecánica de Fluidos, Universidad de Zaragoza*.
- [19] Gottstein, G. (2004). Physical Foundations of Materials Science. *Springer* (Vol. 3).
- [20] Jones, H. R. N. (2005). The Application of Combustion Principles to Domestic Gas Burner Design. *British Gas*.
- [21] Kays, W. M. (1994) Turbulent Prandtl Number - Where Are We? *Journal of Heat Transfer* vol. 116 (2), pp. 284-295.
- [22] Landau, L. D. (1969). Física Teórica Volumen 6. Mecánica de Fluidos. *Reverté*.
- [23] Miettinen, K. M. (1999). Nonlinear Multiobjective Optimization. *Kluwer Academic Publishers*.
- [24] Montañés C. (2015). Development of the Flamelet-Generated Manifold model for the simulation of partially-premixed, non-adiabatic, laminar flames. (Doctoral Thesis). Zaragoza University.
- [25] Poinsot, T. and Veynante, D. (2005). Theoretical and numerical combustion. *R.T. Edwards, Inc.*
- [26] Pope, S. B. (2000). Turbulent Flows. *Cambridge University Press*.
- [27] Vapnik, V., Golowich, S. E. and Smola, A. (1997). Support Vector Method for Function Approximation, Regression Estimation, and Signal Processing. *MIT Press*.
- [28] Warnatz, J., Maas, U. and Dibble, R. (2006). Combustion: Physical and Chemical Fundamentals, Modeling and Simulation, Experiments, Pollutant Formation. *Springer*.
- [29] Williams, F. A. (1985). Combustion Theory. *The Benjamin/Cummings Publishing Company*.
- [30] White, F. M. and Corfield, I. (2006). Viscous fluid flow (Vol. 3). *McGraw-Hill*.